arXiv:1602.05754v1 [math.NA] 18 Feb 2016

FESTUNG: A MATLAB / GNU Octave toolbox for the discontinuous Galerkin method. Part II: Advection operator and slope limiting

Balthasar Reuter[a], Vadym Aizinger[a,*], Manuel Wieland[a], Florian Frank[b], Peter Knabner[a]

[a] *Friedrich–Alexander University of Erlangen–Nürnberg, Department of Mathematics, Cauerstraße 11, 91058 Erlangen, Germany*
[b] *Rice University, Department of Computational and Applied Mathematics, 6100 Main Street – MS 134, Houston, TX 77005-1892, USA*

Abstract

This is the second in a series of papers on implementing a discontinuous Galerkin (DG) method as an open source MATLAB / GNU Octave toolbox. The intention of this ongoing project is to offer a rapid prototyping package for application development using DG methods. The implementation relies on fully vectorized matrix / vector operations and is comprehensively documented. Particular attention was paid to maintaining a direct mapping between discretization terms and code routines as well as to supporting the full code functionality in GNU Octave. The present work focuses on a two-dimensional time-dependent linear advection equation with space / time-varying coefficients, and provides a general order implementation of several slope limiting schemes for the DG method.

Keywords: MATLAB, GNU Octave, discontinuous Galerkin method, slope limiting, vectorization, open source, advection operator

1. Introduction

The development milestones for the MATLAB / GNU Octave toolbox *FESTUNG* (*F*inite *E*lement *S*imulation *T*oolbox for *UN*structured *G*rids) available at [1, 2] run somewhat counter to the history of the development of the discontinuous Galerkin (DG) methods. Thus, our first paper in series [3] introduced a local discontinuous Galerkin discretization for a time-dependent diffusion equation using the numerical methods introduced in [4]. The current work, however, enhances the package with the functionality for purely hyperbolic equations—namely the original purpose of the DG method proposed by Reed and Hill in [5] and analyzed by Johnson and Pitkäranta in [6]. The reason behind this time inversion is that the numerical and software development technology necessary to produce a fully functional DG solver for hyperbolic equations has to include upwind fluxes and slope limiters—both tasks more complicated to solve in a computationally efficient manner than those needed for a pure diffusion equation.

The continued development of this toolbox still adheres to the same design principles declared in [3]:

1. Design a general-purpose software package using the DG method for a range of standard applications and provide this toolbox as a research and learning tool in the open source format (cf. [1]).
2. Supply a well-documented, intuitive user-interface to ease adoption by a wider community of application and engineering professionals.
3. Relying on the vectorization capabilities of MATLAB / GNU Octave, optimize the computational performance of the toolbox components and demonstrate these software development strategies.
4. Maintain throughout full compatibility with GNU Octave to support users of open source software.

*Corresponding author
Email addresses: reuter@math.fau.de (Balthasar Reuter), aizinger@math.fau.de (Vadym Aizinger), manuel.wieland@studium.uni-erlangen.de (Manuel Wieland), florian.frank@rice.edu (Florian Frank), knabner@math.fau.de (Peter Knabner)

We refer to [3] for a literature review on DG methods and open source packages offering a DG capability. The present work expands the functionality of the numerical solver published in the first paper in series by adding linear advection terms and vertex-based slope limiters of general order. The latter development is particularly interesting, since, to the best of our knowledge, no closed form description of vertex-based slope limiters for general order discretizations are to be found in the literature, even less so implementations of such limiters. In addition to hierarchical vertex-based limiters of Kuzmin [7], this publication and the accompanying code includes an extension of the standard linear vertex-based slope limiter to general order discretizations and a new scheme based on the hierarchical vertex-based limiter but using a stricter limiting strategy. Further additions in this work include a selection of TVD (total variation diminishing) Runge–Kutta methods of orders one, two, and three employed for time discretization instead of a simple implicit Euler method used in the first paper.

The rest of this paper is organized as follows: We introduce the model problem in the remainder of this section and describe its discretization using the DG method in Sec. 2. Section 3 introduces slope limiting algorithms, first, for linear DG discretizations followed by the general order case. Implementation specific details such as reformulation and assembly of matrix blocks as well as numerical results are given in Sec. 4. All routines mentioned in this work are listed and documented in Sec. 5. Section 6 concludes the work and gives future perspectives.

1.1. Model problem

Let $J := (0, t_{\text{end}})$ be a finite time interval and $\Omega \subset \mathbb{R}^2$ a polygonally bounded domain with boundary $\partial\Omega$. We consider the *advection equation* in conservative form

$$\partial_t c(t,\boldsymbol{x}) + \boldsymbol{\nabla}\cdot(\boldsymbol{u}(t,\boldsymbol{x})\, c(t,\boldsymbol{x})) \;=\; f(t,\boldsymbol{x}) \qquad \text{in } J\times\Omega \tag{1a}$$

with time / space-varying coefficients $\boldsymbol{u} : J\times\Omega \to \mathbb{R}^2$ and $f : J\times\Omega \to \mathbb{R}$. A prototype application of (1a) is the advective transport in fluids, i. e., the movement of a solute due to the bulk movement of the fluid, in which case the primary unknown c denotes the solute concentration, $\boldsymbol{u}$ the velocity of the fluid, and f accounts for generation or degradation of c, e. g., by chemical reactions. Equation (1a) is complemented by the following boundary and initial conditions:

$$c \;=\; c_{\text{D}} \qquad \text{on } J\times\partial\Omega_{\text{in}}(t)\,, \tag{1b}$$

$$c \;=\; c^0 \qquad \text{on } \{0\}\times\Omega \tag{1c}$$

with inflow boundary $\partial\Omega_{\text{in}}(t) := \{\boldsymbol{x}\in\partial\Omega \,|\, \boldsymbol{u}(t,\boldsymbol{x})\cdot\boldsymbol{\nu}(\boldsymbol{x}) < 0\}$ and $\boldsymbol{\nu}(\boldsymbol{x})$ denoting the outward unit normal. The outflow boundary $\partial\Omega_{\text{out}}(t)$ is defined as $\partial\Omega_{\text{out}}(t) := \partial\Omega \setminus \partial\Omega_{\text{in}}(t)$; $c^0 : \Omega \to \mathbb{R}_0^+$ and $c_{\text{D}} : J\times\partial\Omega_{\text{in}}(t) \to \mathbb{R}_0^+$ are the given initial and Dirichlet boundary data, respectively.

2. Discretization

2.1. Notation

Before describing the DG scheme for (1) we introduce some notation; an overview can be found in the Section "Index of notation". Let $\mathcal{T}_h = \{T\}$ be a regular family of non-overlapping partitions of Ω into K closed triangles T of characteristic size h such that $\overline{\Omega} = \cup T$. For $T\in\mathcal{T}_h$, let $\boldsymbol{\nu}_T$ denote the unit normal on ∂T exterior to T. Let $\mathcal{E}_\Omega$ denote the set of interior edges, $\mathcal{E}_{\partial\Omega}$ the set of boundary edges, and $\mathcal{E} := \mathcal{E}_\Omega \cup \mathcal{E}_{\partial\Omega} = \{E\}$ the set of all edges (the subscript h is suppressed here). For an interior edge $E\in\mathcal{E}_\Omega$ shared by triangles T^- and T^+, we define the one-sided values of a scalar quantity $w = w(\boldsymbol{x})$ on E by

$$w^-(\boldsymbol{x}) \;:=\; \lim_{\varepsilon\to 0^+} w(\boldsymbol{x} - \varepsilon\,\boldsymbol{\nu}_{T^-}) \qquad \text{and} \qquad w^+(\boldsymbol{x}) \;:=\; \lim_{\varepsilon\to 0^+} w(\boldsymbol{x} - \varepsilon\,\boldsymbol{\nu}_{T^+})\,,$$

respectively. For a boundary edge $E\in\mathcal{E}_{\partial\Omega}$, only the definition on the left is meaningful.

2.2. Variational formulation

Because of the local nature of the DG method, we can formulate the variational system of equations on a triangle-by-triangle basis. To do that, we multiply (1a) by a smooth test function $w : T \to \mathbb{R}$ and integrate by parts over element $T \in \mathcal{T}_h$. This gives us

$$\int_T w\,\partial_t c(t)\,\mathrm{d}\boldsymbol{x} - \int_T \boldsymbol{\nabla} w \cdot \boldsymbol{u}(t)\,c(t)\,\mathrm{d}\boldsymbol{x} + \int_{\partial T} w\,\boldsymbol{u}(t)\,c(t)\cdot\boldsymbol{\nu}_T\,\mathrm{d}s \;=\; \int_T w\,f(t)\,\mathrm{d}\boldsymbol{x}\,.$$

2.3. Semi-discrete formulation

We denote by $\mathbb{P}_p(T)$ the space of complete polynomials of degree at most p on $T \in \mathcal{T}_h$. Let

$$\mathbb{P}_p(\mathcal{T}_h) \;\coloneqq\; \left\{w_h : \overline{\Omega} \to \mathbb{R}\,;\; \forall T \in \mathcal{T}_h,\; w_h|_T \in \mathbb{P}_p(T)\right\}$$

denote the broken polynomial space on the triangulation $\mathcal{T}_h$. For the semi-discrete formulation, we assume that the coefficient functions (for $t \in J$ fixed) are approximated as: $\boldsymbol{u}_h \in [\mathbb{P}_p(\mathcal{T}_h)]^2$ and $f_h(t), c_h^0 \in \mathbb{P}_p(\mathcal{T}_h)$. A specific way to compute these approximations was given in the first paper of the series [3]; here we use the standard L^2-projection into $\mathbb{P}_p(T)$, therefore the accuracy of this approximation improves with increasing polynomial order p. Choosing the same polynomial space for all functions simplifies the implementation and is done in preparation for later applications, in which $\boldsymbol{u}_h$ might be part of the solution of a coupled system. Incorporating the boundary condition (1b), the semi-discrete formulation reads:

Seek $c_h(t) \in \mathbb{P}_p(\mathcal{T}_h)$ such that the following holds for $t \in J$ and $\forall T^- \in \mathcal{T}_h$, $\forall w_h \in \mathbb{P}_p(\mathcal{T}_h)$:

$$\int_{T^-} w_h\,\partial_t c_h(t)\,\mathrm{d}\boldsymbol{x} \;-\; \int_{T^-} \boldsymbol{\nabla} w_h \cdot \boldsymbol{u}_h(t)\,c_h(t)\,\mathrm{d}\boldsymbol{x} \;+\; \int_{\partial T^-} w_h^-\left(\boldsymbol{u}(t)\cdot\boldsymbol{\nu}_{T^-}\right)\hat{c}_h(t)\,\mathrm{d}s \;=\; \int_{T^-} w_h\,f_h(t)\,\mathrm{d}\boldsymbol{x}\,, \tag{2}$$

where the boundary integral is calculated using the upwind-sided value

$$\hat{c}_h(t,\boldsymbol{x})\big|_{\partial T^-} = \left\{\begin{array}{lll} c_h^-(t,\boldsymbol{x}) & \text{if} \quad \boldsymbol{u}(t,\boldsymbol{x})\cdot\boldsymbol{\nu}_{T^-} \geq 0 & \text{(outflow from } T^-\text{)} \\ c_h^+(t,\boldsymbol{x}) & \text{if} \quad \boldsymbol{u}(t,\boldsymbol{x})\cdot\boldsymbol{\nu}_{T^-} < 0 \;\wedge\; \boldsymbol{x} \notin \partial\Omega_{\text{in}} & \text{(inflow into } T^- \text{ from } T^+\text{)} \\ c_{\text{D}}(t,\boldsymbol{x}) & \text{if} \quad \boldsymbol{x} \in \partial\Omega_{\text{in}} & \text{(inflow into } T^- \text{ over } \partial\Omega_{\text{in}}\text{)} \end{array}\right\}.$$

Note that we did not use the approximate representation of the velocity $\boldsymbol{u}_h$ in the boundary integral. This is due to the fact that the L^2-projection on elements may have poor approximation quality on edges and generally produces different values on both sides of the edge ultimately leading to different upwind-sided values and inconsistent flux approximations. Instead we evaluate the normal velocity $\boldsymbol{u}\cdot\boldsymbol{\nu}_T$ in each quadrature point analytically and use the result for both the numerical integration and the determination of the upwind direction as will be demonstrated in Sec. 2.3.4.

Thus far, we used an algebraic indexing style. In the remainder, we switch to a mixture of algebraic and numerical style: for instance, $E_{kn} \in \partial T_k \cap \mathcal{E}_\Omega$ means *all possible* combinations of element indices $k \in \{1,\dots,K\}$ and local edge indices $n \in \{1,2,3\}$ such that E_{kn} lies in $\partial T_k \cap \mathcal{E}_\Omega$. This implicitly fixes the numerical indices which accordingly can be used to index matrices or arrays.

We use a bracket notation followed by a subscript to index matrices and multidimensional arrays. Thus, for an n-dimensional array $\mathbf{X}$, the symbol $[\mathbf{X}]_{i_1,\dots,i_n}$ stands for the component of $\mathbf{X}$ with index i_l in the l-th dimension. As in MATLAB / GNU Octave, a colon is used to abbreviate all indices within a single dimension. For example, $[\mathbf{X}]_{:,:,i_3,\dots,i_n}$ is a two-dimensional array / matrix.

2.3.1. Local basis representation

In contrast to globally continuous basis functions mostly used by the continuous finite element method, the DG basis functions have no continuity constraints across triangle boundaries. Thus a standard DG *basis function* $\varphi_{ki} : \overline{\Omega} \to \mathbb{R}$ is only supported on the triangle $T_k \in \mathcal{T}_h$ (i. e., $\varphi_{ki} = 0$ on $\overline{\Omega} \setminus T_k$) and can be defined arbitrarily while ensuring

$$\forall k \in \{1,\dots,K\}\,, \quad \mathbb{P}_p(T_k) \;=\; \operatorname{span}\left\{\varphi_{ki}\right\}_{i\in\{1,\dots,N_p\}}\,, \qquad \text{where} \quad N_p \;\coloneqq\; \frac{(p+1)(p+2)}{2} \;=\; \binom{p+2}{p} \tag{3}$$

is the number of *local degrees of freedom*. Note that N_p may in general vary from triangle to triangle, but, for simplicity, we assume here a uniform polynomial degree p for every triangle and abbreviate $N := N_p$. Clearly, the number of global degrees of freedom equals KN. Closed-form expressions for orthonormal basis functions on the reference triangle $\hat{T}$ (cf. Sec. 4.1) employed in our implementation up to order two can be found in our first paper [3]. The basis functions up to order four are provided in the routine `phi` and their gradients in `gradPhi`. Bases of even higher order can be constructed, e. g., with the Gram–Schmidt algorithm or by using a three-term recursion relation—the latter is unfortunately not trivial to derive in the case of triangles. Note that these so-called *modal* basis functions $\hat{\varphi}_i$ do *not* posses interpolation properties at nodes unlike Lagrangian / nodal basis functions, which are often used by the continuous finite element or nodal DG methods.

The local concentration c_h and the local velocity $\boldsymbol{u}_h$ on $T_k \in \mathcal{T}_h$ can be represented in terms of the local basis $\{\varphi_{ki}\}_{i\in\{1,\dots,N\}}$:

$$c_h(t,\boldsymbol{x})\big|_{T_k} =: \sum_{j=1}^{N} C_{kj}(t)\,\varphi_{kj}(\boldsymbol{x})\,, \qquad \boldsymbol{u}_h(t,\boldsymbol{x})\big|_{T_k} =: \sum_{j=1}^{N}\sum_{m=1}^{2} U_{kj}^{m}(t)\,\boldsymbol{e}_m\varphi_{kj}(\boldsymbol{x})\,,$$

where $\boldsymbol{e}_m$ denotes the m-th unit vector in $\mathbb{R}^2$. We condense the coefficients associated with unknowns into two-dimensional arrays $\mathbf{C}(t)$ such that $C_{kj}(t) := [\mathbf{C}(t)]_{k,j}$, etc. The symbol $[\mathbf{C}]_{k,:}$ is called *local representation matrix* of c_h on T_k with respect to the basis $\{\varphi_{ki}\}_{i\in\{1,\dots,N\}}$. In a similar way, we express the coefficient functions as linear combinations of the basis functions: On $T_k \in \mathcal{T}_h$, we use the local representation matrices $[\mathbf{C}^0]_{k,:}$ for c_h^0 and $[\mathbf{F}]_{k,:}$ for f_h.

2.3.2. System of equations

Testing (2) with $w_h = \varphi_{ki}$ for $i \in \{1,\dots,N\}$ yields a *time-dependent system of equations* whose contribution from T_k (identified with T_{k^-} in boundary integrals) reads

$$\underbrace{\sum_{j=1}^{N}\partial_t C_{kj}(t)\int_{T_k}\varphi_{ki}\,\varphi_{kj}\,\mathrm{d}\boldsymbol{x}}_{\mathit{I}} \underbrace{-\sum_{j=1}^{N} C_{kj}(t)\sum_{l=1}^{N}\sum_{m=1}^{2} U_{kl}^{m}(t)\int_{T_k}\partial_{x^m}\varphi_{ki}\,\varphi_{kl}\,\varphi_{kj}\,\mathrm{d}\boldsymbol{x}}_{\mathit{II}}$$
$$\underbrace{+\int_{\partial T_{k^-}}\varphi_{k^-i}\left(\boldsymbol{u}(t)\cdot\boldsymbol{\nu}_{k^-}\right)\begin{cases}\displaystyle\sum_{j=1}^{N} C_{k^-j}(t)\,\varphi_{k^-j} & \text{if } \boldsymbol{u}(t)\cdot\boldsymbol{\nu}_{k^-}\geq 0\\ \displaystyle\sum_{j=1}^{N} C_{k^+j}(t)\,\varphi_{k^+j} & \text{if } \boldsymbol{u}(t)\cdot\boldsymbol{\nu}_{k^-}<0\ \wedge\ \boldsymbol{x}\notin\partial\Omega_{\mathrm{in}}\\ c_{\mathrm{D}}(t) & \text{if } \boldsymbol{x}\in\partial\Omega_{\mathrm{in}}\end{cases}\mathrm{d}s}_{\mathit{III}} = \underbrace{\sum_{l=1}^{N} F_{kl}(t)\int_{T_k}\varphi_{ki}\,\varphi_{kl}\,\mathrm{d}\boldsymbol{x}}_{\mathit{IV}}\,, \tag{4}$$

where we abbreviated $\boldsymbol{\nu}_{T_k}$ by $\boldsymbol{\nu}_k$. Written in matrix form, system (4) is then given by

$$\mathbf{M}\,\partial_t\boldsymbol{C} + \underbrace{\left(-\mathbf{G}^1-\mathbf{G}^2+\mathbf{R}\right)}_{=:\,\mathbf{A}(t)}\boldsymbol{C} = \underbrace{\boldsymbol{L}-\boldsymbol{K}_{\mathrm{D}}}_{=:\,\boldsymbol{V}(t)} \tag{5}$$

with the representation vector

$$\boldsymbol{C}(t) := \begin{bmatrix} C_{11}(t) & \cdots & C_{1N}(t) & \cdots & \cdots & C_{K1}(t) & \cdots & C_{KN}(t)\end{bmatrix}^{\mathrm{T}}.$$

The block matrices and the right-hand side vectors of (5) are described in Sections 2.3.3 and 2.3.4. Note that all blocks except for the mass matrix $\mathbf{M}$ are time-dependent (we have suppressed the time arguments here).

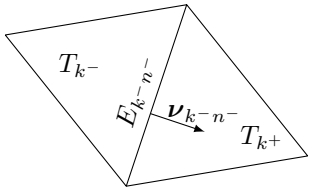


Figure 1: Two triangles adjacent to edge $E_{k^-n^-}$. It holds: $E_{k^-n^-} = E_{k^+n^+}$ and $\boldsymbol{\nu}_{k^-n^-} = -\boldsymbol{\nu}_{k^+n^+}$.

2.3.3. Contributions from area terms I, II, IV

The matrices in the remainder of this section have sparse block structure; by giving definitions for non-zero blocks we tacitly assume a zero fill-in. The *mass matrix* $\mathbf{M} \in \mathbb{R}^{KN\times KN}$ in term I is defined component-wise as

$$[\mathbf{M}]_{(k-1)N+i,(k-1)N+j} \coloneqq \int_{T_k} \varphi_{ki}\,\varphi_{kj}\,.$$

Since the basis functions φ_{ki}, $i \in \{1,\dots,N\}$ are supported only on T_k, $\mathbf{M}$ has a block-diagonal structure

$$\mathbf{M} = \begin{bmatrix} \mathbf{M}_{T_1} & & \\ & \ddots & \\ & & \mathbf{M}_{T_K} \end{bmatrix} \quad \text{with} \quad \mathbf{M}_{T_k} \coloneqq \int_{T_k} \begin{bmatrix} \varphi_{k1}\,\varphi_{k1} & \cdots & \varphi_{k1}\,\varphi_{kN} \\ \vdots & \ddots & \vdots \\ \varphi_{kN}\,\varphi_{k1} & \cdots & \varphi_{kN}\,\varphi_{kN} \end{bmatrix} \mathrm{d}\boldsymbol{x}\,, \tag{6}$$

i. e., it consists of K *local mass matrices* $\mathbf{M}_{T_k} \in \mathbb{R}^{N\times N}$. Henceforth, we write $\mathbf{M} = \operatorname{diag}(\mathbf{M}_{T_1},\dots,\mathbf{M}_{T_K})$.

The block matrices $\mathbf{G}^m \in \mathbb{R}^{KN\times KN}$, $m \in \{1,2\}$ from term *II* are given by

$$[\mathbf{G}^m]_{(k-1)N+i,(k-1)N+j} \coloneqq \sum_{l=1}^{N} U^m_{kl}(t) \int_{T_k} \partial_{x^m}\varphi_{ki}\,\varphi_{kl}\,\varphi_{kj}\,\mathrm{d}\boldsymbol{x}\,.$$

Similarly to $\mathbf{M}$, the matrices $\mathbf{G}^m = \operatorname{diag}(\mathbf{G}^m_{T_1},\dots,\mathbf{G}^m_{T_K})$ are block-diagonal with local matrices

$$\mathbf{G}^m_{T_k} \coloneqq \sum_{l=1}^{N} U^m_{kl}(t) \int_{T_k} \begin{bmatrix} \partial_{x^m}\varphi_{k1}\,\varphi_{kl}\,\varphi_{k1} & \cdots & \partial_{x^m}\varphi_{k1}\,\varphi_{kl}\,\varphi_{kN} \\ \vdots & \ddots & \vdots \\ \partial_{x^m}\varphi_{kN}\,\varphi_{kl}\,\varphi_{k1} & \cdots & \partial_{x^m}\varphi_{kN}\,\varphi_{kl}\,\varphi_{kN} \end{bmatrix} \mathrm{d}\boldsymbol{x}\,. \tag{7}$$

Vector $\boldsymbol{L}(t)$ resulting from *IV* is obtained by multiplication of the representation vector of $f_h(t)$ to the global mass matrix:

$$\boldsymbol{L}(t) = \mathbf{M}\begin{bmatrix} F_{11}(t) & \cdots & F_{1N}(t) & \cdots & \cdots & F_{K1}(t) & \cdots & F_{KN}(t) \end{bmatrix}^{\mathrm{T}}.$$

2.3.4. Contributions from edge term III

Interior Edges $\mathcal{E}_\Omega$. In this section, we consider a fixed triangle $T_k = T_{k^-}$ with an interior edge $E_{k^-n^-} \in \partial T_{k^-} \cap \mathcal{E}_\Omega = \partial T_{k^-} \cap \partial T_{k^+}$ shared by an adjacent triangle T_{k^+} and associated with fixed local edge indices $n^-, n^+ \in \{1,2,3\}$ (cf. Fig. 1).

For a fixed index $i \in \{1,\dots,N\}$, we have a contribution for φ_{k^-i} in a block matrix $\mathbf{R}_\Omega \in \mathbb{R}^{KN\times KN}$

$$\int_{E_{k^-n^-}} \varphi_{k^-i}\left(\boldsymbol{u}(t)\cdot\boldsymbol{\nu}_{k^-n^-}\right) \begin{cases} \sum_{j=1}^{N} C_{k^-j}(t)\,\varphi_{k^-j} & \text{if} \quad \boldsymbol{u}\cdot\boldsymbol{\nu}_{k^-n^-} \geq 0 \\ \sum_{j=1}^{N} C_{k^+j}(t)\,\varphi_{k^+j} & \text{if} \quad \boldsymbol{u}\cdot\boldsymbol{\nu}_{k^-n^-} < 0 \end{cases} \mathrm{d}s\,.$$

This means that, depending on the direction of the velocity field $\boldsymbol{u}(t,\boldsymbol{x})$, we obtain entries in the diagonal or off-diagonal blocks of $\mathbf{R}_\Omega$. Entries in diagonal blocks are then component-wise given by

$$[\mathbf{R}_\Omega]_{(k-1)N+i,(k-1)N+j} \coloneqq \sum_{E_{kn}\in\partial T_k\cap\mathcal{E}_\Omega} \int_{E_{kn}} \varphi_{ki}\,\varphi_{kj}\left(\boldsymbol{u}\cdot\boldsymbol{\nu}_{kn}\right)\delta_{\boldsymbol{u}\cdot\boldsymbol{\nu}_{kn}\geq 0}\,\mathrm{d}s \quad \text{with} \quad \delta_{\boldsymbol{u}\cdot\boldsymbol{\nu}_{kn}\geq 0}(t,\boldsymbol{x}) \coloneqq \begin{cases} 1 & \text{if} \quad \boldsymbol{u}(t,\boldsymbol{x})\cdot\boldsymbol{\nu}_{kn} \geq 0 \\ 0 & \text{if} \quad \boldsymbol{u}(t,\boldsymbol{x})\cdot\boldsymbol{\nu}_{kn} < 0 \end{cases}.$$

(8a)

Entries in off-diagonal blocks in $\mathbf{R}$ are possibly non-zero only for pairs of triangles T_{k^-}, T_{k^+} with $\partial T_{k^-} \cap \partial T_{k^+} \neq \emptyset$ and read

$$[\mathbf{R}_\Omega]_{(k^- -1)N+i,(k^+-1)N+j} \coloneqq \int_{E_{k^-n^-}} \varphi_{k^- i}\, \varphi_{k^+ j} \left(\boldsymbol{u}\cdot\boldsymbol{\nu}_{k^-n^-}\right) \delta_{\boldsymbol{u}\cdot\boldsymbol{\nu}_{k^-n^-}<0}\,\mathrm{d}s \quad \text{with} \quad \delta_{\boldsymbol{u}\cdot\boldsymbol{\nu}_{k^-n^-}<0} \coloneqq 1-\delta_{\boldsymbol{u}\cdot\boldsymbol{\nu}_{k^-n^-}\geq 0}\,. \tag{8b}$$

Boundary Edges $\mathcal{E}_{\partial\Omega}$. Similarly to interior edges we have contributions for a boundary edge $E_{kn} \in \partial T_k \cap \mathcal{E}_{\partial\Omega}$

$$\int_{E_{kn}} \varphi_{ki}\left(\boldsymbol{u}(t)\cdot\boldsymbol{\nu}_{kn}\right) \begin{Bmatrix} \sum_{j=1}^N C_{kj}(t)\,\varphi_{kj} & \text{if} \quad \boldsymbol{u}(t)\cdot\boldsymbol{\nu}_{kn}\geq 0 \\ c_{\mathrm{D}}(t) & \text{if} \quad \boldsymbol{u}(t)\cdot\boldsymbol{\nu}_{kn}<0 \end{Bmatrix} \mathrm{d}s\,.$$

These consist of entries in the block diagonal matrix $\mathbf{R}_{\partial\Omega} \in \mathbb{R}^{KN\times KN}$

$$[\mathbf{R}_{\partial\Omega}]_{(k-1)N+i,(k-1)N+j} \coloneqq \sum_{E_{kn}\in\partial T_k\cap\mathcal{E}_{\partial\Omega}} \int_{E_{kn}} \varphi_{ki}\,\varphi_{kj}\left(\boldsymbol{u}\cdot\boldsymbol{\nu}_{kn}\right)\delta_{\boldsymbol{u}\cdot\boldsymbol{\nu}_{kn}\geq 0}\,\mathrm{d}s\,, \tag{9}$$

and in the right-hand side vector $\boldsymbol{K}_{\mathrm{D}} \in \mathbb{R}^{KN}$

$$[\boldsymbol{K}_{\mathrm{D}}]_{(k-1)N+i} \coloneqq \sum_{E_{kn}\in\partial T_k\cap\mathcal{E}_{\partial\Omega}} \int_{E_{kn}} \varphi_{ki}\, c_{\mathrm{D}}(t)\left(\boldsymbol{u}\cdot\boldsymbol{\nu}_{kn}\right)\delta_{\boldsymbol{u}\cdot\boldsymbol{\nu}_{kn}<0}\,\mathrm{d}s\,. \tag{10}$$

We combine the block matrices $\mathbf{R}_\Omega, \mathbf{R}_{\partial\Omega}$ into a block matrix $\mathbf{R} \in \mathbb{R}^{KN\times KN}$

$$\mathbf{R} \coloneqq \mathbf{R}_\Omega + \mathbf{R}_{\partial\Omega}\,. \tag{11}$$

Since the definition of entries in the diagonal blocks in Eqns. (8a), (9) is the same for both matrices differing only in the set of edges included in the sum, we can disregard the fact whether they are interior or boundary edges and simply assemble the entries for all $E_{kn} \in \partial T_k$.

2.4. Time discretization

The system (5) is equivalent to

$$\mathbf{M}\partial_t \boldsymbol{C}(t) \;=\; \boldsymbol{V}(t) - \mathbf{A}(t)\,\boldsymbol{C}(t) \;=:\; \boldsymbol{S}\big(\boldsymbol{C}(t),t\big) \tag{12}$$

with $\mathbf{A}(t) \in \mathbb{R}^{KN\times KN}$ and right-hand-side vector $\boldsymbol{V}(t) \in \mathbb{R}^{KN}$ as defined in (5).

We discretize system (12) in time using TVD (total variation diminishing) Runge–Kutta methods [8] of orders one, two, and three, which are representatives of the class of SSP (strong stability preserving) Runge–Kutta methods [9]. The advantage of using a time stepping algorithm of such type lies in the guaranteed preservation of the monotonicity of the solution if the DG discretization is also post processed by a slope limiting method.

Let $0 = t^1 < t^2 < \ldots < t_{\mathrm{end}}$ be a not necessarily equidistant decomposition of the time interval J and let $\Delta t^n \coloneqq t^{n+1} - t^n$ denote the time step size. The update scheme of the s-step Runge–Kutta method is given by

$$\begin{aligned} \boldsymbol{C}^{(0)} &= \boldsymbol{C}^n\,, \\ \boldsymbol{C}^{(i)} &= \omega_i\,\boldsymbol{C}^n + (1-\omega_i)\left(\boldsymbol{C}^{(i-1)} + \Delta t^n\,\mathbf{M}^{-1}\boldsymbol{S}^{n+\delta_i}\right), \quad \text{for } i=1,\ldots,s\,, \\ \boldsymbol{C}^{n+1} &= \boldsymbol{C}^{(s)}\,, \end{aligned} \tag{13}$$

where we abbreviated $\boldsymbol{C}^n \coloneqq \boldsymbol{C}(t^n)$ and $\boldsymbol{S}^{n+\delta_i} \coloneqq \boldsymbol{S}(\boldsymbol{C}^{(i-1)}, t^n + \delta_i\Delta t^n)$ with coefficients

$$\begin{aligned} &s=1: && \omega_1 = 0\,, && \delta_1 = 0\,. \\ &s=2: && \omega_1 = 0\,,\ \omega_2 = 1/2\,, && \delta_1 = 0\,,\ \delta_2 = 1\,. \\ &s=3: && \omega_1 = 0\,,\ \omega_2 = 3/4\,,\ \omega_3 = 1/3\,, && \delta_1 = 0\,,\ \delta_2 = 1\,,\ \delta_3 = 1/2\,. \end{aligned}$$

When possible, we choose the order of the time-discretization to be $p+1$, with p being the spatial approximation order, in order to avoid the temporal discretization error dominating the spatial one. Unfortunately, no optimal SSP Runge–Kutta methods higher than order three are known [9], which is why we restrict ourselves to orders one to three for the time discretization.

3. Slope limiting

Slope limiters are a technique to prevent the onset of spurious oscillations that violate the monotonicity preserving property of the piecewise constant part of a DG solution by means of restricting some of the degrees of freedom (generally linear and superlinear) to certain bounds and thus eliminating over- and undershoots. All limiting procedures utilize the fact that the lowest order (piecewise constant) part of a DG solution in explicit TVD time stepping schemes is guaranteed to preserve the monotonicity of the solution and produce no spurious extrema. Using this physically consistent but numerically not very accurate solution part, all slope limiters attempt to modify the full higher order DG solution in a suitable way—on the one hand, to prevent any oscillations and, on the other hand, to preserve as much of the accuracy as possible. The key differences in slope limiters affect the limiting stencil used (edge neighbors, node neighbors, neighbors of the neighbors, etc.), presence of ad hoc parameters, the amount of the introduced numerical diffusion, a strict or less strict preservation of the monotonicity, and the degree of solution degradation in smooth extrema.

Whereas a large literature on slope limiting for piecewise linear DG discretizations exists [10, 11, 12], the limiting of DG solutions with $p \geq 2$ is a much less explored area. The traditional approach to dealing with superlinear DG solutions [13] has been based on ignoring all higher order degrees of freedom on elements on which linear limiting is active. Other methods require a much larger stencil [14, 15] to provide enough information for the reconstruction of higher order derivatives. The hierarchical vertex-based limiters of Kuzmin [16, 7] represent a computationally efficient scheme easily extendable to any discretization order and supporting fully unstructured meshes. These limiters do not guarantee the strict monotonicity of the DG solution, but the violations are small and may be further reduced by simple modifications described in Sec. 3.4.

3.1. Taylor basis representation

Many limiting procedures rely on some fundamental properties of a certain choice of basis, in our case the 2D Taylor basis, which we introduce in a way similar to Kuzmin [16]. Consider the 2D Taylor series expansion of a local solution $c_h \in \mathbb{P}_p(T_k)$,

$$c_h(\boldsymbol{x}) \;=\; \sum_{0\leq|\boldsymbol{a}|\leq p} \partial^{\boldsymbol{a}} c_h(\boldsymbol{x}_{kc}) \frac{(\boldsymbol{x}-\boldsymbol{x}_{kc})^{\boldsymbol{a}}}{\boldsymbol{a}!} \qquad \text{on } T_k \in \mathcal{T}_h \tag{14}$$

about the centroid $\boldsymbol{x}_{kc} = [x^1_{kc}, x^2_{kc}]^{\mathrm{T}}$ of $T_k \in \mathcal{T}_h$ with a two-dimensional multi-index $\boldsymbol{a} = [a^1, a^2]^{\mathrm{T}} \in \mathbb{N}^2_0$, where we use some standard notation for multi-indices $\boldsymbol{a}, \boldsymbol{b} \in \mathbb{N}^2_0$ and $\boldsymbol{x} \in \mathbb{R}^2$:

$$\boldsymbol{a} \pm \boldsymbol{b} = [a^1 \pm b^1, a^2 \pm b^2]^{\mathrm{T}} , \qquad |\boldsymbol{a}| \coloneqq a^1 + a^2 , \qquad \boldsymbol{a}! \coloneqq a^1! a^2! ,$$
$$\boldsymbol{x}^{\boldsymbol{a}} \coloneqq (x^1)^{a^1}(x^2)^{a^2} , \qquad \partial^{\boldsymbol{a}} \coloneqq \partial^{|\boldsymbol{a}|} / \partial (x^1)^{a^1} \, \partial (x^2)^{a^2} .$$

For $v : T_k \to \mathbb{R}$, let $\overline{v} \coloneqq \frac{1}{|T_k|} \int_{T_k} v(\boldsymbol{x}) \, \mathrm{d}\boldsymbol{x}$ denote the integral mean of v on T_k. We express (14) in the equivalent form [17, 18, 19]

$$c_h(\boldsymbol{x}) \;=\; \overline{c}_h + \frac{\partial c_h}{\partial x^1}(\boldsymbol{x}_{kc})(x^1 - x^1_{kc}) + \frac{\partial c_h}{\partial x^2}(\boldsymbol{x}_{kc})(x^2 - x^2_{kc}) + \sum_{2\leq|\boldsymbol{a}|\leq p} \partial^{\boldsymbol{a}} c_h(\boldsymbol{x}_{kc}) \frac{(\boldsymbol{x}-\boldsymbol{x}_{kc})^{\boldsymbol{a}} - \overline{(\boldsymbol{x}-\boldsymbol{x}_{kc})^{\boldsymbol{a}}}}{\boldsymbol{a}!} \quad \text{on } T_k \in \mathcal{T}_h \,. \tag{15}$$

Note that varying any terms in (15) except $\overline{c}_h$ does not affect the mean of $c_h(\boldsymbol{x})$ over T_k.

To be able to identify each term in expansions (14), (15) by a consecutive index, we introduce a linear index mapping $I : \mathbb{N}^2_0 \to \mathbb{N}$ corresponding to any two-dimensional multi-index $\boldsymbol{a} \in \mathbb{N}^2_0$ as

$$I(\boldsymbol{a}) \;=\; N_{|\boldsymbol{a}|-1} + a^2 + 1 \;=\; \frac{|\boldsymbol{a}|(|\boldsymbol{a}|+1)}{2} + a^2 + 1 \tag{16}$$

with $N_p = \dim \mathbb{P}_p(T)$ as defined in (3). We implicitly define $\boldsymbol{a}_j$ such that $\forall j \in \mathbb{N}$, $I(\boldsymbol{a}_j) = j$. The linear indices, polynomial degrees, and corresponding multi-indices up to order four are listed in Table 1. This leads to the following

p	0	1		2			3				4				
$I(\boldsymbol{a}_i)$	1	2	3	4	5	6	7	8	9	10	11	12	13	14	15
$\boldsymbol{a}_i{}^{\mathrm{T}}$	$[0,0]$	$[1,0]$	$[0,1]$	$[2,0]$	$[1,1]$	$[0,2]$	$[3,0]$	$[2,1]$	$[1,2]$	$[0,3]$	$[4,0]$	$[3,1]$	$[2,2]$	$[1,3]$	$[0,4]$

Table 1: Multi-indices *(bottom)*, linear indices *(middle)*, and corresponding polynomial degrees in the Taylor basis (17) *(top)*.

definition of the local Taylor basis [17]:

$$\phi_{k1} = 1\,, \qquad \phi_{k2} = \frac{x_k^1 - x_{\mathrm{kc}}^1}{\Delta(x_k^1)}\,, \qquad \phi_{k3} = \frac{x_k^2 - x_{\mathrm{kc}}^2}{\Delta(x_k^2)}\,, \qquad \phi_{ki} = \frac{(\boldsymbol{x} - \boldsymbol{x}_{\mathrm{kc}})^{\boldsymbol{a}_i} - \overline{(\boldsymbol{x} - \boldsymbol{x}_{\mathrm{kc}})^{\boldsymbol{a}_i}}}{\boldsymbol{a}_i!\,(\Delta \boldsymbol{x}_k)^{\boldsymbol{a}_i}} \quad \text{for} \quad i \geq 4\,. \tag{17}$$

As opposed to the DG basis $\{\varphi_{kj}\}$ (cf. [3], Sec. 2.4.1), the basis $\{\phi_{kj}\}$ cannot be defined on a reference element $\hat{T}$. The scaling by $\Delta \boldsymbol{x}_k = [\Delta(x_k^1), \Delta(x_k^2)]^{\mathrm{T}}$ with $\Delta(x_k^j) := (x_{k,\max}^j - x_{k,\min}^j)/2$, where $x_{k,\max}^j := \max_{i\in\{1,2,3\}} x_{ki}^j$ and $x_{k,\min}^j := \min_{i\in\{1,2,3\}} x_{ki}^j$ are the minimum and maximum values of the corresponding spatial coordinates on T_k, is introduced to obtain a better conditioned operator [17]. The Taylor degrees of freedom are now proportional to the cell mean values $\overline{c}_h$ and derivatives of c_h at the centroid $\boldsymbol{x}_{\mathrm{kc}}$

$$c_h(\boldsymbol{x}) = \overline{c}_h\,\phi_{k1} + \left(\frac{\partial c_h}{\partial x^1}(\boldsymbol{x}_{\mathrm{kc}})\,\Delta\left(x_k^1\right)\right)\phi_{k2}(\boldsymbol{x}) + \left(\frac{\partial c_h}{\partial x^2}(\boldsymbol{x}_{\mathrm{kc}})\,\Delta\left(x_k^2\right)\right)\phi_{k3}(\boldsymbol{x}) + \sum_{i=4}^{N_p}\left(\partial^{\boldsymbol{a}_i} c_h(\boldsymbol{x}_{\mathrm{kc}})\;(\Delta \boldsymbol{x}_k)^{\boldsymbol{a}_i}\right)\phi_{ki}(\boldsymbol{x}) \quad \text{on } T_k \in \mathcal{T}_h\,. \tag{18}$$

Note that the Taylor basis is non-orthogonal on triangular meshes [16], but the cell means are still decoupled from the other degrees of freedom since

$$\int_{T_k} \phi_{k1}^2\,\mathrm{d}\boldsymbol{x} = |T_k|\,, \qquad \int_{T_k} \phi_{k1}\,\phi_{kj}\,\mathrm{d}\boldsymbol{x} = 0 \quad \text{for} \quad j > 1\,.$$

To transform a function c_h from the modal basis representation with representation matrix $\mathbf{C}(t) \in \mathbb{R}^{K\times N}$—as described in Sec. 2.3.1—into a Taylor basis representation with representation matrix $\mathbf{C}^{\mathrm{Taylor}}(t) \in \mathbb{R}^{K\times N}$, we employ the L^2-projection defined locally for $T_k \in \mathcal{T}_h$ by

$$\forall w_h \in \mathbb{P}_p(T_k)\,, \quad \int_{T_k} w_h \left(\sum_{j=1}^{N} C_{kj}(t)\,\varphi_{kj}\right)\mathrm{d}\boldsymbol{x} = \int_{T_k} w_h \left(\sum_{j=1}^{N} C_{kj}^{\mathrm{Taylor}}(t)\,\phi_{kj}\right)\mathrm{d}\boldsymbol{x}\,.$$

Choosing $w_h = \varphi_{ki}$ for $i \in \{1,\ldots,N\}$ we obtain

$$\sum_{j=1}^{N} C_{kj}(t)\int_{T_k}\varphi_{ki}\,\varphi_{kj}\,\mathrm{d}\boldsymbol{x} = \sum_{j=1}^{N} C_{kj}^{\mathrm{Taylor}}(t)\int_{T_k}\varphi_{ki}\,\phi_{kj}\,\mathrm{d}\boldsymbol{x} \quad \Leftrightarrow \quad \mathbf{M}_{T_k}\,[\mathbf{C}]_{k,:} = \mathbf{M}_{T_k}^{\mathrm{DG,Taylor}}\left[\mathbf{C}^{\mathrm{Taylor}}\right]_{k,:}$$

with the local mass matrix $\mathbf{M}_{T_k}$ as defined in Eq. 6 and the local basis transformation matrix

$$\mathbf{M}_{T_k}^{\mathrm{DG,Taylor}} := \int_{T_k}\begin{bmatrix}\varphi_{k1}\,\phi_{k1} & \cdots & \varphi_{k1}\,\phi_{kN}\\ \vdots & \ddots & \vdots\\ \varphi_{kN}\,\phi_{k1} & \cdots & \varphi_{kN}\,\phi_{kN}\end{bmatrix}\mathrm{d}\boldsymbol{x}\,. \tag{19}$$

Using $\mathbf{M}^{\mathrm{DG,Taylor}} := \mathrm{diag}\left(\mathbf{M}_{T_1}^{\mathrm{DG,Taylor}}, \ldots, \mathbf{M}_{T_K}^{\mathrm{DG,Taylor}}\right)$ and representation *vectors* $\boldsymbol{C}, \boldsymbol{C}^{\mathrm{Taylor}} \in \mathbb{R}^{KN}$ we obtain a linear system of equations

$$\mathbf{M}\,\boldsymbol{C} = \mathbf{M}^{\mathrm{DG,Taylor}}\boldsymbol{C}^{\mathrm{Taylor}}\,, \tag{20}$$

which can be employed to transform back-and-forth between both bases.

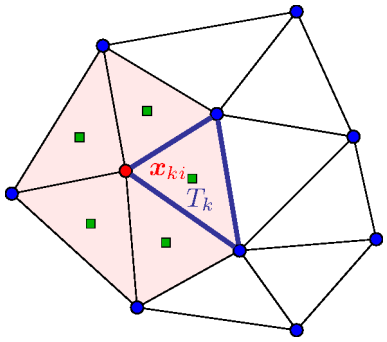


Figure 2: The neighborhood of a vertex $\boldsymbol{x}_{ki} \in T_k$ *(red circle)* considered in Eq. (21) consists of the patch of elements containing $\boldsymbol{x}_{ki}$ *(red area)*. The bounds $c_{ki}^{\min}$, $c_{ki}^{\max}$ from Eq. (22) are determined from all centroid values *(green squares)* within this neighborhood.

3.2. Linear vertex-based limiter

Kuzmin [7, 16] and Aizinger [20] described the vertex-based limiter, which is based on the Barth–Jespersen limiter [21] and improved it further by taking the bounds from all elements containing the vertex instead of taking only edge neighbors of the cell. The goal is to determine the maximum admissible slope for a linear reconstruction of the form

$$c_h(\boldsymbol{x}) = c_{k\mathrm{c}} + \alpha_{ke}\, \boldsymbol{\nabla} c_h(\boldsymbol{x}_{k\mathrm{c}}) \cdot (\boldsymbol{x} - \boldsymbol{x}_{k\mathrm{c}})\,, \qquad 0 \leq \alpha_{ke} \leq 1\,, \quad \boldsymbol{x} \in T_k\,,$$

where we abbreviated the function value $c_{k\mathrm{c}} \coloneqq c_h(\boldsymbol{x}_{k\mathrm{c}})$ in the centroid $\boldsymbol{x}_{k\mathrm{c}}$. The correction factor α_{ke} is chosen such that above reconstruction is bounded in all vertices $\boldsymbol{x}_{ki} \in T_k$ by the minimum and maximum centroid values of all elements containing $\boldsymbol{x}_{ki}$, that is

$$\forall T_k \in \mathcal{T}_h\,, \forall i \in \{1,2,3\}\,, \quad c_{ki}^{\min} \leq c_h(\boldsymbol{x}_{ki}) \leq c_{ki}^{\max} \tag{21}$$

with

$$c_{ki}^{\min} \coloneqq \min_{\{T_l \in \mathcal{T}_h \,|\, \boldsymbol{x}_{ki} \in T_l\}} c_{l\mathrm{c}}\,, \quad c_{ki}^{\max} \coloneqq \max_{\{T_l \in \mathcal{T}_h \,|\, \boldsymbol{x}_{ki} \in T_l\}} c_{l\mathrm{c}} \tag{22}$$

(cf. Fig. 2 for an illustration). To enforce (21), the correction factor α_{ke} is defined as [16]

$$\forall T_k \in \mathcal{T}_h\,, \quad \alpha_{ke} \coloneqq \min_{i \in \{1,2,3\}} \left\{ \begin{array}{lll} (c_{ki}^{\max} - c_{k\mathrm{c}})/(c_{ki} - c_{k\mathrm{c}}) & \text{if} & c_{ki} > c_{ki}^{\max} \\ 1 & \text{if} & c_{ki}^{\min} \leq c_{ki} \leq c_{ki}^{\max} \\ (c_{ki}^{\min} - c_{k\mathrm{c}})/(c_{ki} - c_{k\mathrm{c}}) & \text{if} & c_{ki} < c_{ki}^{\min} \end{array} \right\}\,, \tag{23}$$

where $c_{ki} \coloneqq c_{k\mathrm{c}} + \boldsymbol{\nabla} c_h(\boldsymbol{x}_{k\mathrm{c}}) \cdot (\boldsymbol{x}_{ki} - \boldsymbol{x}_{k\mathrm{c}})$ is the unconstrained linear reconstruction in $\boldsymbol{x}_{ki}$. The limited counterpart of the DG solution (18) becomes then

$$c_h(\boldsymbol{x}) = \overline{c}_h\, \phi_{k1} + \alpha_{ke} \left[\left(\frac{\partial c_h}{\partial x^1}(\boldsymbol{x}_{k\mathrm{c}}) \Delta \left(x_k^1 \right) \right) \phi_{k2}(\boldsymbol{x}) + \left(\frac{\partial c_h}{\partial x^2}(\boldsymbol{x}_{k\mathrm{c}}) \Delta \left(x_k^2 \right) \right) \phi_{k3}(\boldsymbol{x}) \right] \qquad \text{on } T_k \in \mathcal{T}_h\,,$$

i. e., the linear degrees of freedom are scaled by α_{ke}, and any degrees of freedom associated with higher polynomial degrees are set to zero. In the particular case of a linear DG approximation, the limiting can be performed using any hierarchical basis as opposed to higher-order DG solutions that require a Taylor basis representation (see Sec. 3.3). In case of $\alpha_{ke} = 1$, both linear and superlinear degrees of freedom remain unchanged.

3.3. Hierarchical vertex-based limiter

Further improvements by Kuzmin combine the vertex-based or standard Barth–Jespersen limiter with the higher order limiting scheme of Yang and Wang [17], who limit the numerical solution by multiplying all derivatives of

order q by a common correction factor $\alpha_{ke}^{(q)}$ instead of applying the correction only to the linear terms and dropping all higher degrees of freedom. Kuzmin [16] described this scheme in detail for quadratic representations, and here we offer a closed form expression of this limiting procedure for DG discretizations of arbitrary orders.

Let $\mathcal{A}_q := \{\boldsymbol{a} \in \mathbb{N}_0^2 \,\big|\, |\boldsymbol{a}| = q\}$ be the set of all two-dimensional multi-indices of order q. We determine the correction factor $\alpha_{ke}^{(q)}$ for each order $q \le p$ by computing correction factors (23) using the linear vertex-based limiter for all linear reconstructions of derivatives of order $q-1$,

$$\forall\, \boldsymbol{a} \in \mathcal{A}_{q-1}\,, \quad c_{k,\boldsymbol{a},i} := C^{\text{Taylor}}_{k,I(\boldsymbol{a})}\,\phi_{k1}(\boldsymbol{x}_{ki}) + C^{\text{Taylor}}_{k,I(\boldsymbol{a}+[1,0]^{\mathrm{T}})}\,\phi_{k2}(\boldsymbol{x}_{ki}) + C^{\text{Taylor}}_{k,I(\boldsymbol{a}+[0,1]^{\mathrm{T}})}\,\phi_{k3}(\boldsymbol{x}_{ki}) \quad \text{on } T_k \in \mathcal{T}_h\,, \tag{24}$$

where the indices of the corresponding degrees of freedom are given by $I(\boldsymbol{a})$ and the first x^1-derivatives (identified by $I(\boldsymbol{a}+[1,0]^{\mathrm{T}})$) and x^2-derivatives (identified by $I(\boldsymbol{a}+[0,1]^{\mathrm{T}})$). Formally, the correction factor $\alpha_{ke}^{(q)}$ is defined as

$$\alpha_{ke}^{(q)} = \min_{\boldsymbol{a}\in\mathcal{A}_{q-1}} \alpha_{k\boldsymbol{a}}^{(q)}\,, \qquad \text{with} \quad \alpha_{k\boldsymbol{a}}^{(q)} := \min_{i\in\{1,2,3\}} \left\{ \begin{array}{lll} (c^{\max}_{k,\boldsymbol{a},i} - c_{k,\boldsymbol{a},c})/(c_{k,\boldsymbol{a},i} - c_{k,\boldsymbol{a},c}) & \text{if} & c_{\boldsymbol{a},i} > c^{\max}_{\boldsymbol{a},i} \\ 1 & \text{if} & c^{\min}_{k,\boldsymbol{a},i} \le c_{k,\boldsymbol{a},i} \le c^{\max}_{k,\boldsymbol{a},i} \\ (c^{\min}_{k,\boldsymbol{a},i} - c_{k,\boldsymbol{a},c})/(c_{k,\boldsymbol{a},i} - c_{k,\boldsymbol{a},c}) & \text{if} & c_{k,\boldsymbol{a},i} < c^{\min}_{k,\boldsymbol{a},i} \end{array} \right\}, \tag{25}$$

where $c^{\min}_{k,\boldsymbol{a},i}, c^{\max}_{k,\boldsymbol{a},i}$ are defined as in (22). To avoid the loss of accuracy at smooth extrema, the lower order derivatives should be limited by a factor not exceeding that of the higher order derivatives, since lower orders are typically smoother. Beginning with the highest-order degrees of freedom, we compute the correction factors

$$\forall q \ge 1 \quad \alpha_{ke}^{(q)} := \max_{q\le d\le p} \alpha_{ke}^{(d)}\,. \tag{26}$$

Once the correction factor $\alpha_{ke}^{(q)}$ becomes equal to one for some $d > 1$, no further limiting on this element is necessary. The limited solution becomes

$$c_h(\boldsymbol{x}) = \overline{c}_h\,\phi_{k1} + \alpha_{ke}^{(1)}\left(\frac{\partial c_h}{\partial x^1}(\boldsymbol{x}_{kc})\,\Delta\left(x_k^1\right)\right)\phi_{k2}(\boldsymbol{x}) + \alpha_{ke}^{(1)}\left(\frac{\partial c_h}{\partial x^2}(\boldsymbol{x}_{kc})\,\Delta\left(x_k^2\right)\right)\phi_{k3}(\boldsymbol{x}) + \sum_{i=4}^{N} \alpha_{ke}^{(|\boldsymbol{a}_i|)}\left(\partial^{\boldsymbol{a}_i} c_h(\boldsymbol{x}_{kc})\,(\Delta\boldsymbol{x}_k)^{\boldsymbol{a}_i}\right)\phi_{ki}(\boldsymbol{x})\,.$$

3.4. Stricter form of the vertex-based limiter

Our numerical experiments showed that implicitly assuming that higher order derivatives are always smoother than lower order derivatives results in limiting procedures that do not guarantee strict fulfillment of condition (21), especially at discontinuities in the solution. We modified two key components of the limiter presented in the previous section and obtained a limiter that exhibited slightly stronger peak clipping but turned out to be always effective:

1. Instead of employing only the linear reconstruction as given in Eq. (24), we replace $c_{k,\boldsymbol{a},i}$ in the computation of the correction factor in Eq. (25) by the full reconstruction

$$\forall\, \boldsymbol{a} \in \mathcal{A}_{q-1}\,, \quad c_{k,\boldsymbol{a},i} := \sum_{0\le|\boldsymbol{b}|<p-q} C^{\text{Taylor}}_{k,I(\boldsymbol{a}+\boldsymbol{b})}\,\phi_{k,I(\boldsymbol{b})}(\boldsymbol{x}_{ki})\,,$$

 where p is the polynomial degree of the DG solution $c_h(\boldsymbol{x})$.
2. Again, we begin with the highest-order derivative but drop the hierarchical limiting condition (26) and instead apply each correction coefficient $\alpha_{ke}^{(q)}$ immediately to all coefficients corresponding to polynomial degree q or higher. These limited coefficients are then used to compute the next correction coefficient $\alpha_{ke}^{(q-1)}$.

The result of our stricter limiter is

$$c_h(\boldsymbol{x}) = \overline{c}_h\,\phi_{k1} + \alpha_{ke}^{(1)}\left(\frac{\partial c_h}{\partial x^1}(\boldsymbol{x}_{kc})\,\Delta\left(x_k^1\right)\right)\phi_{k2}(\boldsymbol{x}) + \alpha_{ke}^{(1)}\left(\frac{\partial c_h}{\partial x^2}(\boldsymbol{x}_{kc})\,\Delta\left(x_k^2\right)\right)\phi_{k3}(\boldsymbol{x}) + \sum_{i=4}^{N}\left(\alpha_{ke}^{(1)}\cdots\alpha_{ke}^{(|\boldsymbol{a}_i|)}\right)\left(\partial^{\boldsymbol{a}_i} c_h(\boldsymbol{x}_{kc})\,(\Delta\boldsymbol{x}_k)^{\boldsymbol{a}_i}\right)\phi_{ki}(\boldsymbol{x})\,.$$

3.5. Slope limiting in time-dependent problems

For time-dependent problems, the slope limiting procedure is applied to each intermediate solution $\boldsymbol{C}^{(i)}$ in the update scheme (13). However, due to the fact that the Taylor basis is non-orthogonal on triangles—as discussed in Sec. 3.1—an implicit coupling between the spatial derivatives is present and leads to non-smooth spatial variations in the time derivatives of c_h. For that reason, Kuzmin [7] applied the slope limiter not only to the solution of each Runge–Kutta stage but also to the time derivative $\dot{c} := \partial_t c$ and used in addition a filtering procedure that can be interpreted as *selective mass lumping*.

We describe this technique first for a discretization in Taylor basis and extend it then to arbitrary basis representations. Let $\boldsymbol{\Phi}^{\text{Taylor}}$ denote the slope limiting operator that applies any of the above slope limiting procedures to a global representation vector $\boldsymbol{C}^{\text{Taylor}}(t)$ of a solution $c_h(t)$ in Taylor basis representation. The semi-discrete system (12) written in a Taylor basis

$$\mathbf{M}_{\text{C}}\partial_t \boldsymbol{C}^{\text{Taylor}}(t) = \boldsymbol{S}^{\text{Taylor}}\left(\boldsymbol{C}^{\text{Taylor}}(t), t\right)$$

is replaced by

$$\mathbf{M}_{\text{L}}\partial_t \boldsymbol{C}^{\text{Taylor}}(t) = \boldsymbol{S}^{\text{Taylor}}\left(\boldsymbol{\Phi}^{\text{Taylor}}\boldsymbol{C}^{\text{Taylor}}(t), t\right) + \left(\mathbf{M}_{\text{L}} - \mathbf{M}_{\text{C}}\right)\boldsymbol{\Phi}^{\text{Taylor}}\partial_t \boldsymbol{C}^{\text{Taylor}}(t)\,,$$

where $\mathbf{M}_{\text{C}} = \{m_{ij}\}$, $\mathbf{M}_{\text{L}} := \text{diag}\{m_{ii}\}$ denote the full and the lumped mass matrices in Taylor basis (to improve readability, we drop the superscript 'Taylor' here). Note that for the case $\boldsymbol{\Phi}^{\text{Taylor}} = \mathbf{I}$ both formulations are identical. Consequently, update scheme (13) is modified replacing

$$\boldsymbol{C}^{\text{Taylor},(i)} = \omega_i\,\boldsymbol{C}^{\text{Taylor},n} + (1-\omega_i)\left(\boldsymbol{C}^{\text{Taylor},(i-1)} + \Delta t^n\,\dot{\boldsymbol{C}}^{\text{Taylor},(i)}\right) \quad \text{with} \quad \dot{\boldsymbol{C}}^{\text{Taylor},(i)} := \mathbf{M}_{\text{C}}^{-1}\boldsymbol{S}^{\text{Taylor},n+\delta_i}$$

by the selectively lumped and limited update

$$\boldsymbol{C}^{\text{Taylor},(i)} = \boldsymbol{\Phi}^{\text{Taylor}}\left[\omega_i\,\boldsymbol{C}^{\text{Taylor},n} + (1-\omega_i)\left(\boldsymbol{C}^{\text{Taylor},(i-1)} + \Delta t^n\,\tilde{\boldsymbol{C}}^{\text{Taylor},(i)}\right)\right]$$

with

$$\tilde{\boldsymbol{C}}^{\text{Taylor},(i)} = \mathbf{M}_{\text{L}}^{-1}\left[\left(\mathbf{M}_{\text{L}} - \mathbf{M}_{\text{C}}\right)\boldsymbol{\Phi}^{\text{Taylor}}\dot{\boldsymbol{C}}^{\text{Taylor},(i)} + \boldsymbol{S}^{\text{Taylor},n+\delta_i}\right].$$

Although the mass matrix $\mathbf{M}$ in the modal basis is diagonal, the implicit coupling between the spatial x^1- and x^2-derivatives is still present. Only the Taylor basis has vectors coinciding with the coordinate directions, hence, the lumping technique cannot be directly applied to representations in other bases.

To get rid of this implicit coupling of the spatial derivatives in the time derivative of the modal DG basis, we reformulate the lumped time derivative in Taylor basis as

$$\begin{aligned}
\tilde{\boldsymbol{C}}^{\text{Taylor},(i)} &= \mathbf{M}_{\text{L}}^{-1}\mathbf{M}_{\text{L}}\boldsymbol{\Phi}^{\text{Taylor}}\dot{\boldsymbol{C}}^{\text{Taylor},(i)} - \mathbf{M}_{\text{L}}^{-1}\mathbf{M}_{\text{C}}\boldsymbol{\Phi}^{\text{Taylor}}\dot{\boldsymbol{C}}^{\text{Taylor},(i)} + \mathbf{M}_{\text{L}}^{-1}\underbrace{\mathbf{M}_{\text{C}}\mathbf{M}_{\text{C}}^{-1}}_{=\mathbf{I}}\boldsymbol{S}^{\text{Taylor},n+\delta_i} \\
&= \boldsymbol{\Phi}^{\text{Taylor}}\dot{\boldsymbol{C}}^{\text{Taylor},(i)} + \mathbf{M}_{\text{L}}^{-1}\mathbf{M}_{\text{C}}\Big(\underbrace{\mathbf{M}_{\text{C}}^{-1}\boldsymbol{S}^{\text{Taylor},n+\delta_i}}_{=\dot{\boldsymbol{C}}^{\text{Taylor},(i)}} - \boldsymbol{\Phi}^{\text{Taylor}}\dot{\boldsymbol{C}}^{\text{Taylor},(i)}\Big) \\
&= \boldsymbol{\Phi}^{\text{Taylor}}\dot{\boldsymbol{C}}^{\text{Taylor},(i)} + \mathbf{M}_{\text{L}}^{-1}\mathbf{M}_{\text{C}}\Big(\dot{\boldsymbol{C}}^{\text{Taylor},(i)} - \boldsymbol{\Phi}^{\text{Taylor}}\dot{\boldsymbol{C}}^{\text{Taylor},(i)}\Big).
\end{aligned}$$

Using the time derivative in modal basis $\dot{\boldsymbol{C}}^{(i)} = \mathbf{M}^{-1}\boldsymbol{S}^{n+\delta_i}$ and transformation (20), we obtain

$$\tilde{\boldsymbol{C}}^{(i)} = \mathbf{M}^{-1}\mathbf{M}^{\text{DG,Taylor}}\tilde{\boldsymbol{C}}^{\text{Taylor},(i)} = \mathbf{M}^{-1}\mathbf{M}^{\text{DG,Taylor}}\left[\boldsymbol{\Phi}^{\text{Taylor}}\dot{\boldsymbol{C}}^{\text{Taylor},(i)} + \mathbf{M}_{\text{L}}^{-1}\mathbf{M}_{\text{C}}\Big(\dot{\boldsymbol{C}}^{\text{Taylor},(i)} - \boldsymbol{\Phi}^{\text{Taylor}}\dot{\boldsymbol{C}}^{\text{Taylor},(i)}\Big)\right], \tag{27}$$

where $\dot{\boldsymbol{C}}^{\text{Taylor},(i)} := \left(\mathbf{M}^{\text{DG,Taylor}}\right)^{-1}\mathbf{M}\dot{\boldsymbol{C}}^{(i)}$. Thus, the fully modified version of update scheme (13) reads as

$$\begin{aligned}
\boldsymbol{C}^{(0)} &= \boldsymbol{C}^n\,, \\
\boldsymbol{C}^{(i)} &= \boldsymbol{\Phi}\left[\omega_i\,\boldsymbol{C}^n + (1-\omega_i)\left(\boldsymbol{C}^{(i-1)} + \Delta t^n\,\tilde{\boldsymbol{C}}^{(i)}\right)\right] \quad \text{for } \forall i = 1,\ldots,s\,, \\
\boldsymbol{C}^{n+1} &= \boldsymbol{C}^{(s)}\,,
\end{aligned} \tag{28}$$

with $\tilde{\boldsymbol{C}}^{(i)}$ as given in (27) and the slope limiting operator $\boldsymbol{\Phi}$ formally defined as

$$\boldsymbol{\Phi} := \mathbf{M}^{-1}\mathbf{M}^{\text{DG,Taylor}}\boldsymbol{\Phi}^{\text{Taylor}}\left(\mathbf{M}^{\text{DG,Taylor}}\right)^{-1}\mathbf{M}\,. \tag{29}$$

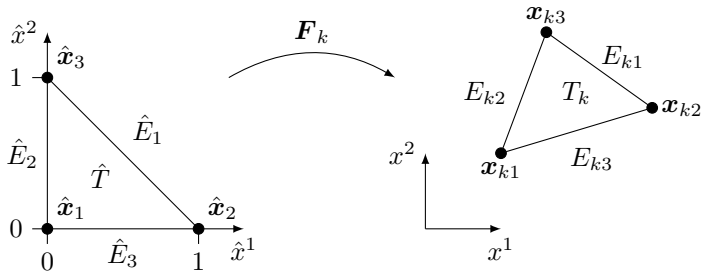


Figure 3: The affine mapping $\boldsymbol{F}_k$ transforms the reference triangle $\hat{T}$ with vertices $\hat{\boldsymbol{x}}_1 = [0, 0]^{\mathrm{T}}$, $\hat{\boldsymbol{x}}_2 = [1, 0]^{\mathrm{T}}$, $\hat{\boldsymbol{x}}_3 = [0, 1]^{\mathrm{T}}$ to the physical triangle T_k with counter-clockwise-ordered vertices $\boldsymbol{x}_{ki}$, $i \in \{1, 2, 3\}$.

3.6. Boundary conditions

Problems can occur when computing the bounds $c_{ki}^{\min}, c_{ki}^{\max}$ in Eq. (21) for control points $\boldsymbol{x}_{ki} \in \partial\Omega_{\mathrm{in}}$ on the Dirichlet boundary. To account for the boundary data in the limiting procedure we include on those control points the boundary value $c_{\mathrm{D}}(t^n + \delta_i \Delta t^n, \boldsymbol{x}_{ki})$ in the minimum/maximum-operation in Eq. (22) for $\alpha_{ke}^{(1)}$ when applying the slope limiting operator $\boldsymbol{\Phi}$ in Eq. (28).

4. Implementation

An extensive documentation on our data structures, grid, etc. can be found in the first paper of the series [3]. These explanations are not reproduced here; greater detail is provided for routines first introduced in the present work.

4.1. Backtransformation to the reference triangle

We are using a back transformation to the reference triangle $\hat{T} = \{(0, 0), (1, 0), (0, 1)\}$ defined by an affine mapping

$$\boldsymbol{F}_k : \quad \hat{T} \ni \hat{\boldsymbol{x}} \mapsto \mathbf{B}_k \hat{\boldsymbol{x}} + \boldsymbol{x}_{k1} = \boldsymbol{x} \in T_k\,, \qquad \text{with} \quad \mathbb{R}^{2\times 2} \ni \mathbf{B}_k := \left[\boldsymbol{x}_{k2} - \boldsymbol{x}_{k1} \,\middle|\, \boldsymbol{x}_{k3} - \boldsymbol{x}_{k1}\right], \tag{30}$$

for any triangle $T_k = \{\boldsymbol{x}_{k1}, \boldsymbol{x}_{k2}, \boldsymbol{x}_{k3}\} \in \mathcal{T}_h$ (see Fig. 3). It holds $0 < \det \mathbf{B}_k = 2|T_k|$. Any function $w : T_k \to \mathbb{R}$ implies $\hat{w} : \hat{T} \to \mathbb{R}$ by $\hat{w} = w \circ \boldsymbol{F}_k$, i. e., $w(\boldsymbol{x}) = \hat{w}(\hat{\boldsymbol{x}})$. The transformation of the gradient is obtained by the chain rule:

$$\boldsymbol{\nabla} \;=\; (\hat{\boldsymbol{\nabla}} \boldsymbol{F}_k)^{-\mathrm{T}}\, \hat{\boldsymbol{\nabla}}\,, \tag{31}$$

where we abbreviated $\hat{\boldsymbol{\nabla}} = [\partial_{\hat{x}^1}, \partial_{\hat{x}^2}]^{\mathrm{T}}$. This results in transformation formulas for integrals over an element T_k or an edge $E_{kn} \subset T_k$ for a function $w : \Omega \to \mathbb{R}$

$$\int_{T_k} w(\boldsymbol{x})\,\mathrm{d}\boldsymbol{x} \;=\; \frac{|T_k|}{|\hat{T}|} \int_{\hat{T}} w \circ \boldsymbol{F}_k(\hat{\boldsymbol{x}})\,\mathrm{d}\hat{\boldsymbol{x}} \;=\; 2|T_k| \int_{\hat{T}} w \circ \boldsymbol{F}_k(\hat{\boldsymbol{x}})\,\mathrm{d}\hat{\boldsymbol{x}} \;=\; 2|T_k| \int_{\hat{T}} \hat{w}(\hat{\boldsymbol{x}})\,\mathrm{d}\hat{\boldsymbol{x}}\,, \tag{32a}$$

$$\int_{E_{kn}} w(\boldsymbol{x})\,\mathrm{d}\boldsymbol{x} \;=\; \frac{|E_{kn}|}{|\hat{E}_n|} \int_{\hat{E}_n} w \circ \boldsymbol{F}_k(\hat{\boldsymbol{x}})\,\mathrm{d}\hat{\boldsymbol{x}} \;=\; \frac{|E_{kn}|}{|\hat{E}_n|} \int_{\hat{E}_n} \hat{w}(\hat{\boldsymbol{x}})\,\mathrm{d}\hat{\boldsymbol{x}}\,. \tag{32b}$$

4.2. Numerical integration

As an alternative to the symbolic integration functions provided by MATLAB, we implemented a quadrature integration functionality for triangle and edge integrals.

Since we transform all integrals on $T_k \in \mathcal{T}_h$ to the reference triangle $\hat{T}$ (cf. Sec. 4.1), it is sufficient to define the quadrature rules on $\hat{T}$ (which, of course, can be rewritten to apply for every physical triangle $T = \boldsymbol{F}_T(\hat{T})$):

$$\int_{\hat{T}} \hat{g}(\hat{\boldsymbol{x}})\,\mathrm{d}\hat{\boldsymbol{x}} \;\approx\; \sum_{r=1}^{R} \omega_r\, \hat{g}(\hat{\boldsymbol{q}}_r) \tag{33}$$

with R *quadrature points* $\hat{\boldsymbol{q}}_r \in \hat{T}$ and *quadrature weights* $\omega_r \in \mathbb{R}$. The *order* of a quadrature rule is the largest integer s such that (33) is *exact* for polynomials $g \in \mathbb{P}_s(\hat{T})$. Note that we exclusively rely on quadrature rules with positive weights and quadrature points located strictly in the interior of $\hat{T}$ and not on $\partial\hat{T}$. The rules used in the implementation are found in the routine `quadRule2D`. An overview of quadrature rules on triangles can be found in the "Encyclopaedia of Cubature Formulas" [22]. For edge integration, we rely on standard Gauss quadrature rules of required order.

The integrals in (4) contain integrands that are polynomials of maximum order $3p-1$ on triangles and of maximum order $3p$ on edges. Using quadrature integration, one could choose rules that integrate all such terms exactly; however, sufficient accuracy can be achieved with quadrature rules that are exact for polynomials of order $2p$ on triangles and $2p+1$ on edges (cf. [23]).

4.3. Assembly

The aim of this section is to transform the terms required to build the block matrices in (5) to the reference triangle $\hat{T}$ and then to evaluate those either via numerical quadrature or analytically. The assembly of block matrices from local contributions is then performed in vectorized operations.

For the implementation, we need the explicit form for the components of the mappings $\boldsymbol{F}_k : \hat{T} \to T_k$ and their inverses $\boldsymbol{F}_k^{-1} : T_k \to \hat{T}$ as defined in (30). Recalling that $0 < \det \mathbf{B}_k = 2|T_k|$ (cf. Sec. 4.1) we obtain

$$\boldsymbol{F}_k(\hat{\boldsymbol{x}}) = \begin{bmatrix} B_k^{11}\,\hat{x}^1 + B_k^{12}\,\hat{x}^2 + a_{k1}^1 \\ B_k^{21}\,\hat{x}^1 + B_k^{22}\,\hat{x}^2 + a_{k1}^2 \end{bmatrix} \qquad \text{and} \qquad \boldsymbol{F}_k^{-1}(\boldsymbol{x}) = \frac{1}{2\,|T_k|} \begin{bmatrix} B_k^{22}\,(x^1 - a_{k1}^1) - B_k^{12}\,(x^2 - a_{k1}^2) \\ B_k^{11}\,(x^2 - a_{k1}^2) - B_k^{21}\,(x^1 - a_{k1}^1) \end{bmatrix}.$$

From (31) we obtain the component-wise rule for the gradient in $\boldsymbol{x} \in T_k$:

$$\begin{bmatrix} \partial_{x^1} \\ \partial_{x^2} \end{bmatrix} = \frac{1}{2\,|T_k|} \begin{bmatrix} B_k^{22}\,\partial_{\hat{x}^1} - B_k^{21}\,\partial_{\hat{x}^2} \\ B_k^{11}\,\partial_{\hat{x}^2} - B_k^{12}\,\partial_{\hat{x}^1} \end{bmatrix}. \tag{34}$$

Similarly to the first paper in series [3], we make extensive use of the Kronecker product $\mathbf{A} \otimes \mathbf{B}$ of two matrices $\mathbf{A} = [a_{ij}] \in \mathbb{R}^{m_a \times n_a}$, $\mathbf{B} = [b_{kl}] \in \mathbb{R}^{m_b \times n_b}$ defined as

$$\mathbf{A} \otimes \mathbf{B} \coloneqq \Big[a_{ij}\mathbf{B}\Big] \in \mathbb{R}^{m_a m_b \times n_a n_b}. \tag{35}$$

In the following, we present the necessary transformation for all blocks of system (5) and name the corresponding MATLAB / GNU Octave routines that can be found in Sec. 5.

4.3.1. Assembly of $\mathbf{M}$

Using the transformation rule (32a), the following holds for the local mass matrix $\mathbf{M}_{T_k}$ as defined in (6):

$$\mathbf{M}_{T_k} = 2|T_k|\,\hat{\mathbf{M}} \qquad \text{with} \qquad \hat{\mathbf{M}} \coloneqq \int_{\hat{T}} \begin{bmatrix} \hat{\varphi}_1\,\hat{\varphi}_1 & \cdots & \hat{\varphi}_1\,\hat{\varphi}_N \\ \vdots & \ddots & \vdots \\ \hat{\varphi}_N\,\hat{\varphi}_1 & \cdots & \hat{\varphi}_N\,\hat{\varphi}_N \end{bmatrix}, \tag{36}$$

where $\hat{\mathbf{M}} \in \mathbb{R}^{N\times N}$ is the representation of the local mass matrix on the reference triangle $\hat{T}$. With (6) we see that the global mass matrix $\mathbf{M}$ can be expressed as a Kronecker product of a matrix containing the areas $|T_k|$ and the local matrix $\hat{\mathbf{M}}$:

$$\mathbf{M} = \begin{bmatrix} \mathbf{M}_{T_1} & & \\ & \ddots & \\ & & \mathbf{M}_{T_K} \end{bmatrix} = 2 \begin{bmatrix} |T_1| & & \\ & \ddots & \\ & & |T_K| \end{bmatrix} \otimes \hat{\mathbf{M}}.$$

In the corresponding assembly routine `assembleMatElemPhiPhi`, the sparse block-diagonal matrix is generated using the command `spdiags` with the list `g.areaT` (cf. [3]).

4.3.2. Assembly of $\mathbf{G}^m$

Application of the product rule, (32a), and (34) gives us

$$\int_{T_k} \partial_{x^1} \varphi_{ki}\, \varphi_{kl}\, \varphi_{kj} \;=\; B_k^{22}\,[\hat{\mathbf{G}}]_{i,j,l,1} - B_k^{21}\,[\hat{\mathbf{G}}]_{i,j,l,2}\,, \qquad \int_{T_k} \partial_{x^2} \varphi_{ki}\, \varphi_{kl}\, \varphi_{kj} \;=\; -B_k^{12}\,[\hat{\mathbf{G}}]_{i,j,l,1} + B_k^{11}\,[\hat{\mathbf{G}}]_{i,j,l,2}$$

with a multidimensional array $\hat{\mathbf{G}} \in \mathbb{R}^{N\times N\times N\times 2}$ representing the transformed integral on the reference triangle $\hat{T}$:

$$[\hat{\mathbf{G}}]_{i,j,l,m} \;\coloneqq\; \int_{\hat{T}} \partial_{\hat{x}^m} \hat{\varphi}_i\, \hat{\varphi}_j\, \hat{\varphi}_l\,, \quad \text{for } m \in \{1,2\}\,. \tag{37}$$

Now we can express the local matrix $\mathbf{G}^1_{T_k}$ from (7) as

$$\begin{aligned}\mathbf{G}^1_{T_k} &= \sum_{l=1}^{N} U^1_{kl}(t) \left(B_k^{22} \int_{\hat{T}} \begin{bmatrix} \partial_{\hat{x}^1}\hat{\varphi}_1\hat{\varphi}_1\hat{\varphi}_l & \cdots & \partial_{\hat{x}^1}\hat{\varphi}_1\hat{\varphi}_N\hat{\varphi}_l \\ \vdots & \ddots & \vdots \\ \partial_{\hat{x}^1}\hat{\varphi}_N\hat{\varphi}_1\hat{\varphi}_l & \cdots & \partial_{\hat{x}^1}\hat{\varphi}_N\hat{\varphi}_N\hat{\varphi}_l \end{bmatrix} - B_k^{21} \int_{\hat{T}} \begin{bmatrix} \partial_{\hat{x}^2}\hat{\varphi}_1\hat{\varphi}_1\hat{\varphi}_l & \cdots & \partial_{\hat{x}^2}\hat{\varphi}_1\hat{\varphi}_N\hat{\varphi}_l \\ \vdots & \ddots & \vdots \\ \partial_{\hat{x}^2}\hat{\varphi}_N\hat{\varphi}_1\hat{\varphi}_l & \cdots & \partial_{\hat{x}^2}\hat{\varphi}_N\hat{\varphi}_N\hat{\varphi}_l \end{bmatrix} \right) \\ &= \sum_{l=1}^{N} U^1_{kl}(t) \left(B_k^{22} [\hat{\mathbf{G}}]_{:,:,l,1} - B_k^{21} [\hat{\mathbf{G}}]_{:,:,l,2} \right)\end{aligned}$$

and analogously $\mathbf{G}^2_{T_k}$. With $\mathbf{G}^m = \operatorname{diag}(\mathbf{G}^m_{T_1}, \ldots, \mathbf{G}^m_{T_K})$ we can vectorize over all triangles using the Kronecker product as done in the routine `assembleMatElemDphiPhiFuncDiscVec`. We would like to point out that this is identical to the assembly of $\mathbf{G}^m$ in our first paper [3] except for the vectorial coefficient function; however, the respective section had some typos, above is the corrected version. Additionally, in the assembly routine the wrong component of the normal vector was used for the assembly of $\mathbf{G}^m$. Corrected and up-to-date versions of the code can be found in our Github-repository [2].

4.3.3. Assembly of $\mathbf{R}$

To ease the assembly of $\mathbf{R}$ we split the global matrix as given in (11) into a block-diagonal part and a remainder so that $\mathbf{R} = \mathbf{R}^{\text{diag}} + \mathbf{R}^{\text{offdiag}}$ holds. We first consider the block-diagonal entries of $\mathbf{R}$ given in Eqns. (8a), (9) and transform the integral terms to the n-th edge of the reference triangle $\hat{E}_n$:

$$\begin{aligned}\int_{E_{kn}} \varphi_{ki}\, \varphi_{kj} \left(\boldsymbol{u}\cdot\boldsymbol{\nu}_{kn}\right) \delta_{\boldsymbol{u}\cdot\boldsymbol{\nu}_{kn}\geq 0}\,\mathrm{d}\boldsymbol{x} &= \frac{|E_{kn}|}{|\hat{E}_n|} \int_{\hat{E}_n} \hat{\varphi}_i\, \hat{\varphi}_j \left((\boldsymbol{u}\circ \boldsymbol{F}_k(\hat{\boldsymbol{x}}))\cdot\boldsymbol{\nu}_{kn}\right) \delta_{\boldsymbol{u}\cdot\boldsymbol{\nu}_{kn}\geq 0}\,\mathrm{d}\hat{\boldsymbol{x}} \\ &= \frac{|E_{kn}|}{|\hat{E}_n|} \int_0^1 \hat{\varphi}_i\circ\hat{\boldsymbol{\gamma}}_n(s)\,\hat{\varphi}_j\circ\hat{\boldsymbol{\gamma}}_n(s) \Big(\underbrace{(\boldsymbol{u}\circ\boldsymbol{F}_k\circ\hat{\boldsymbol{\gamma}}_n(s))}_{=:\,\hat{\boldsymbol{u}}_{kn}(s)}\cdot\boldsymbol{\nu}_{kn}\Big)\,\delta_{\hat{\boldsymbol{u}}_{kn}\cdot\boldsymbol{\nu}_{kn}\geq 0}\,|\hat{\boldsymbol{\gamma}}_n'(s)|\,\mathrm{d}s \\ &\approx |E_{kn}| \sum_{r=1}^{R} \omega_r \underbrace{\hat{\varphi}_i\circ\hat{\boldsymbol{\gamma}}_n(q_r)\,\hat{\varphi}_j\circ\hat{\boldsymbol{\gamma}}_n(q_r)}_{=:[\hat{\mathbf{R}}^{\text{diag}}]_{i,j,n,r}} \left(\boldsymbol{u}_{kn}(q_r)\cdot\boldsymbol{\nu}_{kn}\right)\delta_{\hat{\boldsymbol{u}}_{kn}\cdot\boldsymbol{\nu}_{kn}\geq 0}\,,\end{aligned} \tag{38}$$

where we used transformation rule (32b), quadrature rule (33), and $|\hat{\boldsymbol{\gamma}}_n'(s)| = |\hat{E}_n|$. The explicit forms of the mappings $\hat{\boldsymbol{\gamma}}_n : [0,1] \to \hat{E}_n$ can be easily derived:

$$\hat{\boldsymbol{\gamma}}_1(s) \;\coloneqq\; \begin{bmatrix} 1-s \\ s \end{bmatrix}, \qquad \hat{\boldsymbol{\gamma}}_2(s) \;\coloneqq\; \begin{bmatrix} 0 \\ 1-s \end{bmatrix}, \qquad \hat{\boldsymbol{\gamma}}_3(s) \;\coloneqq\; \begin{bmatrix} s \\ 0 \end{bmatrix}. \tag{39}$$

Thus, we can assemble the global matrix using the Kronecker product

$$\mathbf{R}^{\text{diag}} \coloneqq \sum_{n=1}^{3}\sum_{r=1}^{R} \omega_r \begin{bmatrix} |E_{1n}| & & \\ & \ddots & \\ & & |E_{Kn}| \end{bmatrix} \circ \begin{bmatrix} (\hat{\boldsymbol{u}}_{1n}(q_r)\cdot\boldsymbol{\nu}_{1n})\,\delta_{\hat{\boldsymbol{u}}_{1n}\cdot\boldsymbol{\nu}_{1n}\geq 0} & & \\ & \ddots & \\ & & (\hat{\boldsymbol{u}}_{Kn}(q_r)\cdot\boldsymbol{\nu}_{Kn})\,\delta_{\hat{\boldsymbol{u}}_{Kn}\cdot\boldsymbol{\nu}_{Kn}\geq 0} \end{bmatrix} \otimes \left[\hat{\mathbf{R}}^{\text{diag}}\right]_{:,:,n,r},$$

where '$\circ$' denotes the Hadamard product.

Next, we consider the off-diagonal blocks of $\mathbf{R}$ stored in $\mathbf{R}^{\text{offdiag}}$. For an interior edge $E_{k^-n^-} = E_{k^+n^+} \in \partial T_{k^-} \cap \partial T_{k^+}$, $n^-, n^+ \in \{1,2,3\}$, we obtain analogously:

$$
\begin{aligned}
&\int_{E_{k^-n^-}} \varphi_{k^-i}\, \varphi_{k^+j} \left(\boldsymbol{u}\cdot\boldsymbol{\nu}_{k^-n}\right) \delta_{\boldsymbol{u}\cdot\boldsymbol{\nu}_{k^-n}<0}\,\mathrm{d}\boldsymbol{x} \\
&\quad= \frac{|E_{k^-n^-}|}{|\hat{E}_{n^-}|} \int_{\hat{E}_{n^-}} \hat{\varphi}_i\, \varphi_{k^+j} \circ \overbrace{\boldsymbol{F}_{k^+} \circ \boldsymbol{F}_{k^+}^{-1}}^{=\mathrm{I}} \circ \boldsymbol{F}_{k^-}(\hat{\boldsymbol{x}}) \left((\boldsymbol{u}\circ\boldsymbol{F}_{k^-}(\hat{\boldsymbol{x}}))\cdot\boldsymbol{\nu}_{k^-n^-}\right) \delta_{\boldsymbol{u}\cdot\boldsymbol{\nu}_{k^-n^-}<0}\,\mathrm{d}\hat{\boldsymbol{x}} \\
&\quad= \frac{|E_{k^-n^-}|}{|\hat{E}_{n^-}|} \int_{\hat{E}_{n^-}} \hat{\varphi}_i\, \hat{\varphi}_j \circ \boldsymbol{F}_{k^+}^{-1} \circ \boldsymbol{F}_{k^-}(\hat{\boldsymbol{x}}) \left((\boldsymbol{u}\circ\boldsymbol{F}_{k^-}(\hat{\boldsymbol{x}}))\cdot\boldsymbol{\nu}_{k^-n^-}\right) \delta_{\boldsymbol{u}\cdot\boldsymbol{\nu}_{k^-n^-}<0}\,\mathrm{d}\hat{\boldsymbol{x}} \\
&\quad= |E_{k^-n^-}| \int_0^1 \hat{\varphi}_i \circ \hat{\boldsymbol{\gamma}}_{n^-}(s)\, \hat{\varphi}_j \circ \boldsymbol{F}_{k^+}^{-1} \circ \boldsymbol{F}_{k^-} \circ \hat{\boldsymbol{\gamma}}_{n^-}(s) \left(\hat{\boldsymbol{u}}_{k^-n^-}(s)\cdot\boldsymbol{\nu}_{k^-n^-}\right) \delta_{\hat{\boldsymbol{u}}_{k^-n^-}\cdot\boldsymbol{\nu}_{k^-n^-}<0}\,\mathrm{d}s\,.
\end{aligned}
$$

Note that $\boldsymbol{F}_{k^+}^{-1} \circ \boldsymbol{F}_{k^-}$ maps from $\hat{T}$ to $\hat{T}$. Since we compute a line integral, the integration domain is further restricted to an edge $\hat{E}_{n^-}$, $n^- \in \{1,2,3\}$ and its co-domain to an edge $\hat{E}_{n^+}$, $n^+ \in \{1,2,3\}$. As a result, this integration can be boiled down to nine possible maps between the sides of the reference triangle expressed as

$$
\hat{\boldsymbol{\vartheta}}_{n^-n^+}: \quad \hat{E}_{n^-} \ni \hat{\boldsymbol{x}} \mapsto \hat{\boldsymbol{\vartheta}}_{n^-n^+}(\hat{\boldsymbol{x}}) = \boldsymbol{F}_{k^+}^{-1} \circ \boldsymbol{F}_{k^-}(\hat{\boldsymbol{x}}) \in \hat{E}_{n^+}
$$

for an arbitrary index pair $\{k^-, k^+\}$ as described above. The closed-form expressions of the nine cases are given in our first paper [3]. We apply quadrature rule (33) and define $\hat{\mathbf{R}}^{\text{offdiag}} \in \mathbb{R}^{N\times N\times 3\times 3\times R}$ by

$$
\left[\hat{\mathbf{R}}^{\text{offdiag}}\right]_{i,j,n^-,n^+,r} := \hat{\varphi}_i \circ \hat{\boldsymbol{\gamma}}_{n^-}(q_r)\, \hat{\varphi}_j \circ \hat{\boldsymbol{\vartheta}}_{n^-n^+} \circ \hat{\boldsymbol{\gamma}}_{n^-}(q_r) \tag{40}
$$

and thus arrive at

$$
\begin{aligned}
\mathbf{R}^{\text{offdiag}} := \sum_{n^-=1}^{3}\sum_{n^+=1}^{3}\sum_{r=1}^{R} \omega_r
&\begin{bmatrix}
0 & \delta_{E_{1n^-}=E_{2n^+}} & \cdots & \cdots & \delta_{E_{1n^-}=E_{Kn^+}} \\
\delta_{E_{2n^-}=E_{1n^+}} & 0 & \ddots & & \vdots \\
\vdots & \ddots & \ddots & \ddots & \vdots \\
\vdots & & \ddots & 0 & \delta_{E_{(K-1)n^-}=E_{Kn^+}} \\
\delta_{E_{Kn^-}=E_{1n^+}} & \cdots & \cdots & \delta_{E_{Kn^-}=E_{(K-1)n^+}} & 0
\end{bmatrix} \\
&\circ \begin{bmatrix}
|E_{1n^-}|\,(\hat{\boldsymbol{u}}_{1n^-}\cdot\boldsymbol{\nu}_{1n^-})\,\delta_{\hat{\boldsymbol{u}}_{1n^-}\cdot\boldsymbol{\nu}_{1n^-}<0} & \cdots & |E_{1n^-}|\,(\hat{\boldsymbol{u}}_{1n^-}\cdot\boldsymbol{\nu}_{1n^-})\,\delta_{\hat{\boldsymbol{u}}_{1n^-}\cdot\boldsymbol{\nu}_{1n^-}<0} \\
\vdots & & \vdots \\
|E_{Kn^-}|\,(\hat{\boldsymbol{u}}_{Kn^-}\cdot\boldsymbol{\nu}_{Kn^-})\,\delta_{\hat{\boldsymbol{u}}_{Kn^-}\cdot\boldsymbol{\nu}_{Kn^-}<0} & \cdots & |E_{Kn^-}|\,(\hat{\boldsymbol{u}}_{Kn^-}\cdot\boldsymbol{\nu}_{Kn^-})\,\delta_{\hat{\boldsymbol{u}}_{Kn^-}\cdot\boldsymbol{\nu}_{Kn^-}<0}
\end{bmatrix} \otimes [\hat{\mathbf{R}}^{\text{offdiag}}]_{:,:,n^-,n^+,r}\,.
\end{aligned}
$$

The sparsity structure for off-diagonal blocks depends on the numbering of mesh entities and is given for each combination of n^- and n^+ by the list `markE0TE0T`. Due to the upwind flux in the edge integrals, it is not possible here to include the quadrature rule directly in the element-blocks $\hat{\mathbf{R}}^{\text{offdiag}}$ as opposed to the assembly of element integrals and the assembly routines for edges in the first paper [3]. Implementing the assembly with above formulation is possible but expensive, since the global matrix would have to to be built for every quadrature point. Instead we make use of the fact that the sparsity structure is the same for every quadrature point as we solely rely on the element numbering and do not account for the upwind direction when determining the structure of $\mathbf{R}^{\text{offdiag}}$. We define a tensor of block vectors $\tilde{\mathbf{R}}^{\text{offdiag}} \in \mathbb{R}^{KN\times N\times 3\times 3}$

$$
\left[\tilde{\mathbf{R}}^{\text{offdiag}}\right]_{(k-1)N+1:kN,:,n-,n+} := \sum_{r=1}^{R} \omega_r
\begin{bmatrix}
|E_{1n^-}|\,(\hat{\boldsymbol{u}}_{1n^-}\cdot\boldsymbol{\nu}_{1n^-})\,\delta_{\hat{\boldsymbol{u}}_{1n^-}\cdot\boldsymbol{\nu}_{1n^-}<0} \\
\vdots \\
|E_{Kn^-}|\,(\hat{\boldsymbol{u}}_{Kn^-}\cdot\boldsymbol{\nu}_{Kn^-})\,\delta_{\hat{\boldsymbol{u}}_{Kn^-}\cdot\boldsymbol{\nu}_{Kn^-}<0}
\end{bmatrix} \otimes [\hat{\mathbf{R}}^{\text{offdiag}}]_{:,:,n^-,n^+,r}\,.
$$

For $m_b = rm_a, r \in \mathbb{N}$, let

$$
\cdot \otimes_{\mathrm{V}} \cdot: \quad \mathbb{R}^{m_a\times n_a} \times \mathbb{R}^{m_b\times n_b} \ni (\mathbf{A},\mathbf{B}) \mapsto \mathbf{A}\otimes_{\mathrm{V}}\mathbf{B} := \left[[\mathbf{A}]_{i,j}\,[\mathbf{B}]_{(i-1)r:ir,:}\right] \in \mathbb{R}^{m_b\times n_a n_b} \tag{41}
$$

be an operator which can be interpreted as a Kronecker product (cf. Eq. (35)) that takes a different right-hand side for every row of the left-hand side and is implemented in the routine `kronVec`. This allows us to write

$$\mathbf{R}^{\text{offdiag}} = \sum_{n^-=1}^{3}\sum_{n^+=1}^{3} \begin{bmatrix} 0 & \delta_{E_{1n^-}=E_{2n^+}} & \dots & \dots & \delta_{E_{1n^-}=E_{Kn^+}} \\ \delta_{E_{2n^-}=E_{1n^+}} & 0 & \ddots & & \vdots \\ \vdots & \ddots & \ddots & \ddots & \vdots \\ \vdots & & \ddots & 0 & \delta_{E_{(K-1)n^-}=E_{Kn^+}} \\ \delta_{E_{Kn^-}=E_{1n^+}} & \dots & \dots & \delta_{E_{Kn^-}=E_{(K-1)n^+}} & 0 \end{bmatrix} \otimes_{\mathrm{V}} \left[\tilde{\mathbf{R}}^{\text{offdiag}}\right]_{:,:,n-,n+} ,$$

which omits the expensive assembly of the global matrix in every quadrature point.

The routine `assembleMatEdgePhiPhiValUpwind` assembles the matrices $\mathbf{R}^{\text{diag}}$ and $\mathbf{R}^{\text{offdiag}}$ directly into $\mathbf{R}$ with a code very similar to the formulation above. To avoid repeated computation of the normal velocity $\boldsymbol{u}\cdot\boldsymbol{\nu}_{kn}$, we evaluate it once in all quadrature points on each edge using the globally continuous function $\boldsymbol{u}(t,\boldsymbol{x})$ and store it in a dedicated variable `vNormalOnQuadEdge`, which is then employed in the decision of the upwind direction using $\delta_{\boldsymbol{u}\cdot\boldsymbol{\nu}_{kn}\geq 0}$ and $\delta_{\boldsymbol{u}\cdot\boldsymbol{\nu}_{kn}<0}$ as well as the normal velocity in the assembly of $\mathbf{R}$ and $\boldsymbol{K}_{\mathrm{D}}$.

4.3.4. Assembly of $\boldsymbol{K}_{\mathrm{D}}$

The entries of $\boldsymbol{K}_{\mathrm{D}}$ in (10) are transformed using transformation rule (32b) and mapping (39)

$$\begin{aligned} [\boldsymbol{K}_{\mathrm{D}}]_{(k-1)N+i} &= \sum_{E_{kn}\in\partial T_k\cap\mathcal{E}_{\partial\Omega}} \int_{E_{kn}} \varphi_{ki}\, c_{\mathrm{D}}(t)\left(\boldsymbol{u}\cdot\nu_{kn}^m\right)\delta_{\boldsymbol{u}\cdot\nu_{kn}^m<0}\,\mathrm{d}\boldsymbol{x} \\ &= \sum_{E_{kn}\in\partial T_k\cap\mathcal{E}_{\partial\Omega}} \frac{|E_{kn}|}{|\hat{E}_n|}\int_{\hat{E}_n} \hat{\varphi}_i\, c_{\mathrm{D}}(t,\boldsymbol{F}_k(\hat{\boldsymbol{x}}))\left((\boldsymbol{u}\circ\boldsymbol{F}_k(\hat{\boldsymbol{x}}))\cdot\nu_{kn}^m\right)\delta_{\boldsymbol{u}\cdot\nu_{kn}^m<0}\,\mathrm{d}\hat{\boldsymbol{x}} \\ &= \sum_{E_{kn}\in\partial T_k\cap\mathcal{E}_{\partial\Omega}} |E_{kn}|\int_0^1 \hat{\varphi}_i\circ\hat{\boldsymbol{\gamma}}_n(s)\, c_{\mathrm{D}}(t,\boldsymbol{F}_k\circ\hat{\boldsymbol{\gamma}}_n(s))\left(\hat{\boldsymbol{u}}_{kn}(s)\cdot\nu_{kn}^m\right)\delta_{\hat{\boldsymbol{u}}_{kn}\cdot\nu_{kn}^m<0}\,\mathrm{d}s\,, \end{aligned}$$

where we again implicitly assumed the application of $\boldsymbol{F}_k$ and $\hat{\boldsymbol{\gamma}}_n$ to $\delta_{\boldsymbol{u}\cdot\boldsymbol{\nu}_{kn}\geq 0}$. This integral is then approximated using a 1D quadrature rule (33) on the reference interval $(0,1)$

$$[\boldsymbol{K}_{\mathrm{D}}]_{(k-1)N+i} \approx \sum_{E_{kn}\in\partial T_k\cap\mathcal{E}_{\partial\Omega}} |E_{kn}|\sum_{r=1}^{R}\omega_r\hat{\varphi}_i\circ\hat{\boldsymbol{\gamma}}_n(q_r)\, c_{\mathrm{D}}(t,\boldsymbol{F}_k\circ\hat{\boldsymbol{\gamma}}_n(q_r))\left(\hat{\boldsymbol{u}}_{kn}(q_r)\cdot\nu_{kn}^m\right)\delta_{\hat{\boldsymbol{u}}_{kn}\cdot\nu_{kn}^m<0}$$

allowing to vectorize the computation over all triangles and resulting in the routine `assembleVecEdgePhiIntFuncContVal`.

4.4. Slope limiters

For the implementation of the slope limiters described in Sec. 3, three parts must be considered:

1. The assembly of the transformation matrix $\mathbf{M}^{\mathrm{DG,Taylor}}$ from Eq. (19);
2. the slope limiters themselves;
3. the selective mass lumping in the limiting of time-derivatives, as explained in Sec. 3.5.

4.4.1. Assembly of $\mathbf{M}^{\mathrm{DG,Taylor}}$

The entries in $\mathbf{M}^{\mathrm{DG,Taylor}}$ are transformed using transformation rule (32a), and the integral is then approximated using a 2D quadrature rule (33) on the reference triangle $\hat{T}$

$$\left[\mathbf{M}^{\mathrm{DG,Taylor}}\right]_{(k-1)N+i,(k-1)N+j} = \int_{T_k}\varphi_{ki}\,\phi_{kj}\,\mathrm{d}\boldsymbol{x} = 2|T_k|\int_{\hat{T}}\hat{\varphi}_i\,\phi_{kj}\circ\boldsymbol{F}_k(\hat{\boldsymbol{x}})\,\mathrm{d}\hat{\boldsymbol{x}} \approx 2|T_k|\sum_{r=1}^{R}\hat{\varphi}_i(\boldsymbol{q}_r)\,\phi_{kj}\circ\boldsymbol{F}_k(\boldsymbol{q}_r)\,.$$

Recall that we cannot define the Taylor basis (17) on the reference triangle $\hat{T}$ since the basis functions depend directly on the physical coordinates of the element. The assembly is vectorized over all triangles resulting in the routine `assembleMatElemPhiDiscPhiTaylor`. Matrices $\mathbf{M}^{\mathrm{DG,Taylor}}$ and $\mathbf{M}$ assembled in Sec. 4.3.1 are then used in the routines `projectDataDisc2DataTaylor` and `projectDataTaylor2DataDisc` to transform the representation matrix between the modal and Taylor basis—as explained in Sec. 3.1—by solving system (20).

4.4.2. Slope limiting operators

The slope limiters themselves are implemented in a generic manner according to Sec. 3. Beginning with the highest-order derivatives, we evaluate the linear or the full reconstruction of these derivatives at all control points $\boldsymbol{x}_{ki}$. These values along with the centroid values are used to determine the minimum and maximum values $c_{ki}^{\min}$ and $c_{ki}^{\max}$ (see Eq. (21)) for each control point and, from these, the element-wise correction factors α_e according to Eq. (23) or (25) are calculated. This is implemented in routine `computeVertexBasedLimiter`. Depending on the limiter type, this value is then applied to a certain subset of degrees of freedom, and the computation is repeated for the next lower-order derivatives. The full slope limiting operators $\boldsymbol{\Phi}$, $\boldsymbol{\Phi}^{\text{Taylor}}$ are provided by the functions `applySlopeLimiterDisc` or `applySlopeLimiterTaylor`, respectively.

To overcome numerical problems for cases where $c_{ki} \approx c_{ki}^{\max}$ or $c_{ki} \approx c_{ki}^{\min}$, we modify Eqs. (23) and (25) so that the condition for cases 1 and 3 are modified to $c_{ki} > c_{ki}^{\max} - \epsilon$ and $c_{ki} < c_{ki}^{\min} + \epsilon$ for a small $0 < \epsilon \in \mathbb{R}$. Additionally, we increase the absolute value of the denominators in cases 1 and 3 by ϵ, i. e., add or subtract ϵ, respectively. This makes our limiter slightly more strict than the one given by condition (21); $\epsilon = 10^{-8}$ has been found to be a suitable value for double precision computations. Moreover, we enforce $0 \leq \alpha_{ke} \leq 1$ to overcome cases where the division by a number close to zero might lead to values $\alpha_{ke} > 1$. To reduce execution time, we perform the necessary evaluation of the Taylor basis functions in all vertices only once and store the result in a global variable that is used in the slope limiting routines. This is implemented in `computeTaylorBasesV0T`.

4.4.3. Limiting time-derivatives

To obtain the selectively lumped time-derivative $\tilde{\boldsymbol{C}}^{(i)}$ required for update scheme (28), we compute the discrete time derivative $\dot{\boldsymbol{C}}^{(i)}$ as given in Sec. 3.5 and transform it to a Taylor basis representation using Eq. (20) (implemented in routine `projectDataDisc2DataTaylor`). We compute the stationary matrix

$$\mathbf{M}^{\text{corr}} := \mathbf{M}_{\text{L}}^{-1}\mathbf{M}$$

in the beginning (which is computationally cheap, since $\mathbf{M}_{\text{L}}$ is a diagonal matrix) and calculate the selectively lumped time-derivative $\tilde{\boldsymbol{C}}^{\text{Taylor},(i)}$ from Equation (27). Backtransformation to the modal DG basis is again cheap, since it requires only the inverse of the diagonal matrix $\mathbf{M}$ (implemented in `projectDataTaylor2DataDisc`) to produce the selectively lumped time-derivative $\tilde{\boldsymbol{C}}^{(i)}$. Each intermediate solution $\boldsymbol{C}^{(i)}$ in update scheme (28) is then obtained by applying the slope limiting operator $\boldsymbol{\Phi}$ implemented in `applySlopeLimiterDisc`.

4.5. Numerical results

4.5.1. Analytical convergence test

The code is verified by showing that the numerically estimated orders of convergences match the analytically predicted ones for prescribed smooth solutions. To verify the spatial discretization, we restrict ourselves to the stationary version of (1) and investigate the impact of different slope limiting schemes on the convergence order. The effectiveness of the slope limiters is verified in the next section.

We choose the exact solution $c(\boldsymbol{x}) := \cos(7x^1)\cos(7x^2)$ and velocity field $\boldsymbol{u}(\boldsymbol{x}) := [\exp((x^1 + x^2)/2), \exp((x^1 - x^2)/2)]^{\text{T}}$ on the domain $\Omega := (0,1)^2$. The data c_{D} and f are derived analytically by inserting c and $\boldsymbol{u}$ into (1). We then compute the solution c_{h_j} for a sequence of increasingly finer meshes with element sizes h_j, where the coarsest grid $\mathcal{T}_{h_0}$ covering Ω is an irregular grid, and each finer grid is obtained by regular refinement of its predecessor. The *discretization error* $\|c_h(t) - c(t)\|_{L^2(\Omega)}$ at time $t \in J$ is computed as the L^2-norm of the difference between the discrete solution $c_h(t)$ and the analytical solution $c(t)$, as it was described in detail in our first paper [3]. Table 2 contains the results demonstrating the experimental order of convergence α estimated using

$$\alpha := \ln\left(\frac{\|c_{h_{j-1}} - c\|_{L^2(\Omega)}}{\|c_{h_j} - c\|_{L^2(\Omega)}}\right) \Big/ \ln\left(\frac{h_{j-1}}{h_j}\right).$$

The interesting points to compare in Table 2 are the errors for different limiting schemes. Whereas the linear approximation does not get limited at all on finer grids—indicating that the vertex-based limiters are able to distinguish between smooth and non-smooth solutions given sufficient mesh resolution, the case of higher order approximation warrants a closer look. First of all, the linear limiter takes a heavy toll on the higher order degrees of freedom:

limiter	p / j	0 $\|c_h - c\|$	0 α	1 $\|c_h - c\|$	1 α	2 $\|c_h - c\|$	2 α	3 $\|c_h - c\|$	3 α	4 $\|c_h - c\|$	4 α
none	0	3.64e–1	—	5.44e–1	—	6.98e–1	—	2.73e–1	—	2.21e–1	—
	1	5.64e–1	–0.63	4.25e–1	0.36	1.32e–1	2.40	8.51e–2	1.68	1.46e–2	3.92
	2	3.49e–1	0.69	1.28e–1	1.73	2.82e–2	2.23	6.10e–3	3.80	1.25e–3	3.54
	3	2.49e–1	0.49	3.65e–2	1.81	3.15e–3	3.16	3.87e–4	3.98	4.58e–5	4.77
	4	1.73e–1	0.53	8.29e–3	2.14	3.68e–4	3.10	2.39e–5	4.02	1.51e–6	4.92
	5	1.09e–1	0.66	1.93e–3	2.11	4.50e–5	3.03	1.50e–6	4.00	4.80e–8	4.97
	6	6.35e–2	0.78	4.71e–4	2.03	5.59e–6	3.01	9.36e–8	4.00	1.51e–9	4.99
linear	0	—	—	5.15e–1	—	7.21e–1	—	4.60e–1	—	5.27e–1	—
	1	—	—	4.53e–1	0.19	3.55e–1	1.02	3.54e–1	0.38	3.59e–1	0.55
	2	—	—	1.64e–1	1.47	1.34e–1	1.41	1.51e–1	1.23	1.47e–1	1.29
	3	—	—	4.53e–2	1.85	3.12e–2	2.10	3.12e–2	2.27	3.12e–2	2.23
	4	—	—	8.76e–3	2.37	4.48e–3	2.80	4.46e–3	2.81	4.46e–3	2.81
	5	—	—	1.98e–3	2.14	6.20e–4	2.85	6.19e–4	2.85	6.19e–4	2.85
	6	—	—	4.74e–4	2.07	7.63e–5	3.02	7.61e–5	3.02	7.61e–5	3.02
hier. vert. based	0	—	—	5.15e–1	—	6.98e–1	—	2.73e–1	—	2.21e–1	—
	1	—	—	4.53e–1	0.19	2.47e–1	1.50	2.57e–1	0.09	1.33e–1	0.73
	2	—	—	1.64e–1	1.47	1.06e–1	1.22	5.89e–2	2.12	5.10e–2	1.38
	3	—	—	4.53e–2	1.85	7.87e–3	3.76	4.02e–3	3.87	3.17e–3	4.01
	4	—	—	8.76e–3	2.37	6.39e–4	3.62	6.16e–5	6.03	6.53e–6	8.92
	5	—	—	1.98e–3	2.14	5.32e–5	3.59	2.62e–6	4.56	1.08e–7	5.92
	6	—	—	4.74e–4	2.07	5.94e–6	3.16	1.17e–7	4.48	5.48e–9	4.30
strict	0	—	—	5.15e–1	—	6.84e–1	—	3.28e–1	—	3.56e–1	—
	1	—	—	4.53e–1	0.19	3.79e–1	0.85	3.69e–1	–0.17	3.54e–1	0.00
	2	—	—	1.64e–1	1.47	1.14e–1	1.74	6.74e–2	2.45	6.15e–2	2.53
	3	—	—	4.53e–2	1.85	1.23e–2	3.21	1.20e–2	2.49	1.16e–2	2.40
	4	—	—	8.76e–3	2.37	1.15e–3	3.41	8.99e–4	3.74	8.85e–4	3.72
	5	—	—	1.98e–3	2.14	1.19e–4	3.27	1.33e–4	2.76	1.33e–4	2.74
	6	—	—	4.74e–4	2.07	6.64e–6	4.17	1.09e–6	6.93	1.13e–6	6.88

Table 2: Discretization errors measured in $L^2(\Omega)$ and estimated orders of convergences for different polynomial degrees and limiter types. We have $h_j = \frac{1}{3 \cdot 2^j}$ and $K = 36 \cdot 4^j$ triangles in the jth refinement level.

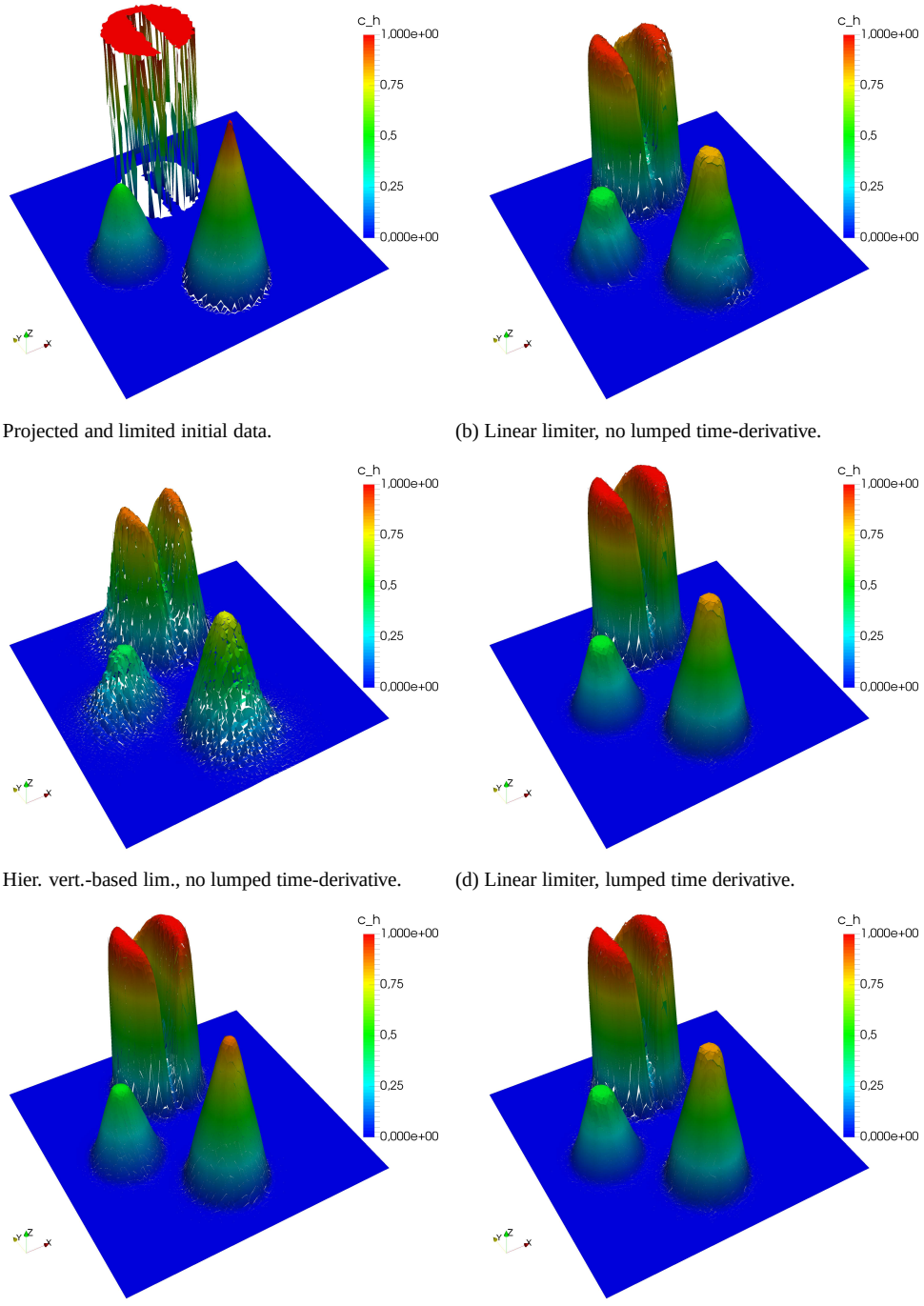
quadratic, cubic, and quartic solutions produce virtually the same error, thus negating the effect of a more accurate DG solution. The strict limiter seems to flatten out after the cubic approximation, thus gaining one order of convergence on the linear limiter. The hierarchical limiter of Kuzmin, however, appears to perform very well for all tested meshes and approximation orders having a very small effect on the errors of the analytical test case.

4.5.2. Solid body rotation

As a benchmark problem, we use solid body rotation test proposed by LeVeque [24], which is often used to investigate limiter performance [7, 13]. It consists of a slotted cylinder, a sharp cone, and a smooth hump (see Figure 4a) that are placed in a square domain $\Omega = [0, 1]^2$ and transported by a time-independent velocity field $\boldsymbol{u}(\boldsymbol{x}) = [0.5 - x^2, x^1 - 0.5]^{\mathrm{T}}$ in a counterclockwise rotation over $J = (0, 2\pi)$. With $r = 0.0225$ and $G(\boldsymbol{x}, \boldsymbol{x}_0) := \frac{1}{0.15}\|\boldsymbol{x} - \boldsymbol{x}_0\|_2$, we choose initial data satisfying

$$c^0(\boldsymbol{x}) = \left\{ \begin{array}{lll} 1 & \text{if} \quad (x^1 - 0.5)^2 + (x^2 - 0.75)^2 \leq r & \text{(slotted cylinder)} \\ & \quad \wedge (x^1 \leq 0.475 \vee x^1 \geq 0.525 \vee x^2 \geq 0.85) & \\ 1 - G(\boldsymbol{x}, [0.5, 0.25]^{\mathrm{T}}) & \text{if} \quad (x^1 - 0.5)^2 + (x^2 - 0.25)^2 \leq r & \text{(sharp cone)} \\ \frac{1}{4}(1 + \cos(\pi G(\boldsymbol{x}, [0.25, 0.5]^{\mathrm{T}}))) & \text{if} \quad (x^1 - 0.25)^2 + (x^2 - 0.5)^2 \leq r & \text{(smooth hump)} \\ 0 & \text{otherwise} & \end{array} \right\}$$

and zero boundary $c_{\mathrm{D}} = 0$ and right-hand side $f = 0$.



(a) Projected and limited initial data.

(b) Linear limiter, no lumped time-derivative.

(c) Hier. vert.-based lim., no lumped time-derivative.

(d) Linear limiter, lumped time derivative.

(e) Hier. vert.-based limiter, lumped time derivative.

(f) Strict limiter, lumped time derivative.

Figure 4: Visualization of the DG solutions with $p = 2$ at end time $t_{\text{end}} = 2\pi$.

First, we would like to emphasize the huge improvement of the solution when applying Kuzmin's selectively lumped time-stepping scheme (cf. Sec. 3.5), which reduces numerical diffusion and peak clipping, as visible in the intersection lines in Fig. 5 and the 3D visualization (Figs. 4b–4e) and results in a smaller error (see Tab. 3). Without this technique, the implicit coupling of the derivatives renders the higher order limiter inferior to the linear limiter.

The results for the different slope limiters (see Fig. 4d–4f) when applying the lumped time-stepping scheme are similar with all limiters producing errors in the same range (see Tab. 3). The linear vertex based limiter exhibits significantly stronger peak clipping than the higher order limiters in the intersection lines of Fig. 6. When looking at the slotted cylinder the strict limiter outperforms the others, producing less fill-in in the slot and better preserving the shape of the cylinder. Also, the total error is lowest for the strict limiter.

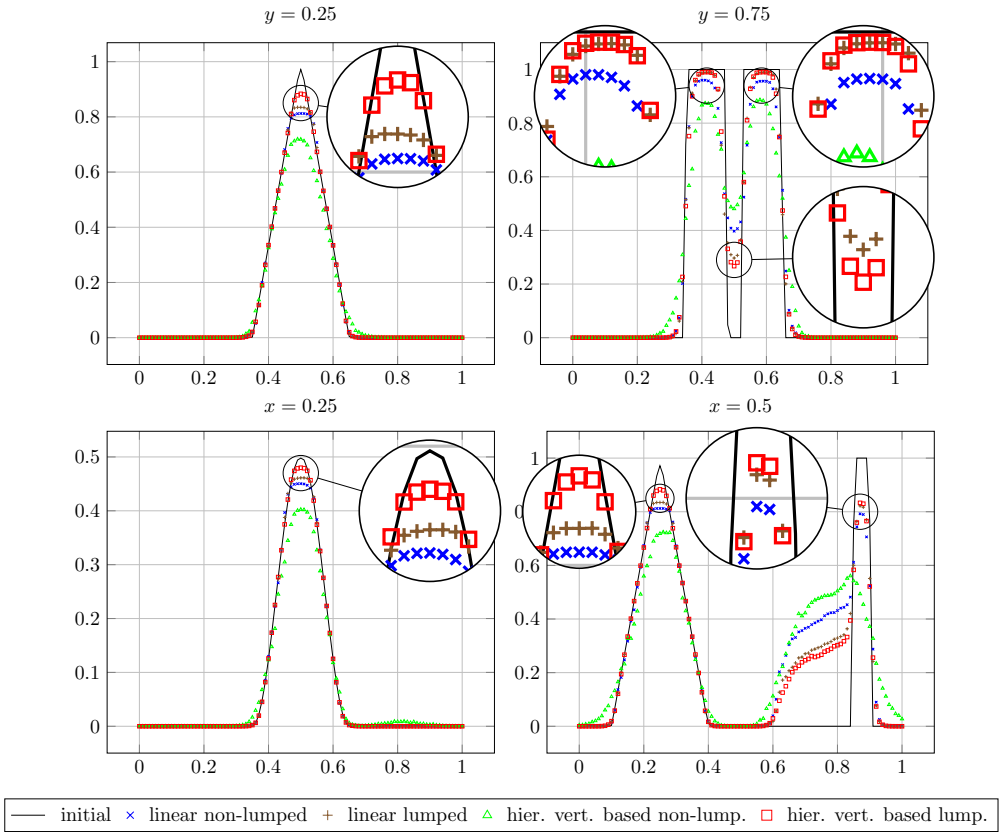


Figure 5: Intersection lines of the DG solution with $p = 2$ at end time $t_{\text{end}} = 2\pi$ with and without the selectively lumped time-derivative, as described in Section. 3.5. The large deviation of the solutions from the initial data in the lower right plot are due to fill-in of the slot in the cylinder.

For polynomial degrees $p \geq 2$ the solution might still violate the bounds along the edges when using only control points in the vertices of the element for the slope limiting procedure. When evaluating the numerical fluxes, these values are transported to the neighboring elements and can lead to cell averages lying outside of the initial bounds in the next time step. Table 3 shows that all limiter types suffer from this, however these small violations of the bounds usually smooth out over time due to the effects of numerical diffusion and do not introduce numerical problems. The linear limiter is the only that preserves the upper bound but comes at the price of stronger peak-clipping. To effectively restrict the solution to these bounds for $p = 2$, additional control points on the edges are necessary, which leads to a significant increase in numerical diffusion, hence this is not a suitable technique.

5. Register of Routines

We list here all routines of our implementation that were added since the first paper [3] in alphabetic order. For the reason of compactness, we waive the check for correct function arguments, e. g., by means of routines as `assert`. However, it is strongly recommended to catch exceptions if the code is to be extended. The argument `g` is always

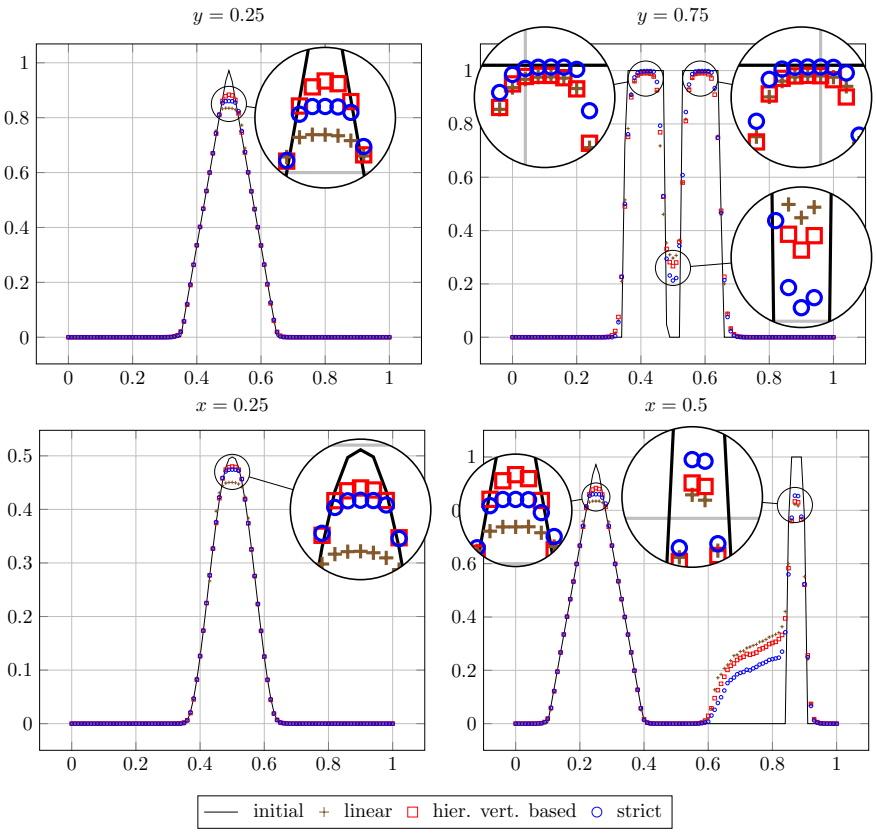


Figure 6: Intersection lines of the DG solution with $p = 2$ at end time $t_{\text{end}} = 2\pi$ when applying the lumped time-stepping scheme (cf. Sec. 3.5). Compared are solutions with the different limiters described in Section 3.

	non-lumped		*lumped*		
	linear	hier. vertex-based	linear	hier. vertex-based	strict
$\min_k c_h(\boldsymbol{x}_{kc})$	0.00	–1.11e–5	–3.95e–10	–6.18e–5	–6.42e–4
$\min_{k,i} c_h(\boldsymbol{x}_{ki})$	–2.93e–2	–2.47e–2	–9.53e–3	–9.69e–3	–9.79e–16
$\min_{k,j} c_h(\boldsymbol{x}_{e,kj})$	–3.32e–8	–4.28e–3	–1.18e–7	–4.28e–3	–5.35e–3
$\max_k c_h(\boldsymbol{x}_{kc})$	1.00000	1.00000	1.00000	1.00000	1.00142
$\max_{k,i} c_h(\boldsymbol{x}_{ki})$	1.00000	1.00915	1.00000	1.01760	1.00000
$\max_{k,j} c_h(\boldsymbol{x}_{e,kj})$	1.00000	1.00014	1.00000	1.00297	1.00296
$\|c_h(0) - c^0\|_{L^2(\Omega)}$	3.73e–2	3.66e–2	3.73e–2	3.66e–2	3.66e–2
$\|c_h(t_{\text{end}}) - c^0\|_{L^2(\Omega)}$	8.18e–2	1.15e–1	7.38e–2	7.40e–2	7.07e–2

Table 3: Minimum and maximum values in centroids $\boldsymbol{x}_{kc}$, nodes $\boldsymbol{x}_{ki}$, and edge midpoints $\boldsymbol{x}_{e,kj}$ with $p = 2$ over the entire simulation time $J = (0, 2\pi)$. Two last rows give the L^2-errors of the slope-limited projection of initial data and the end solution when compared to the analytical initial data.

a `struct` representing the triangulation $\mathcal{T}_h$, the argument `N` is always the number of local basis functions N. A script that demonstrates the application of the presented routines is given in `mainAdvection.m`.

Additionally, we recommend using Laurent Sorbers slightly faster implementation of the Kronecker product [25] for `sparse` matrices from MATLAB File Exchange[1] to speed up the computation. Note that this implementation is only suitable for `logical` and `double` matrices.

[1] http://www.mathworks.com/matlabcentral/fileexchange/

`dataDisc = applySlopeLimiterDisc(g, dataDisc, markV0TbdrD, dataV0T, globM, globMDiscTaylor, type)` implements the slope limiting operator $\mathbf{\Phi}$, as given in Eq. (29) with the chosen limiter type given as a string in `type`. Parameter `dataDisc` is the representation matrix in modal DG basis, `markV0TbdrD` is a logical matrix marking all Dirichlet boundary nodes for which boundary data is given in `dataV0T`.

```
function dataDisc = applySlopeLimiterDisc(g,dataDisc,markV0TbdrD,dataV0T,globM,globMDiscTaylor,type)
dataTaylor = projectDataDisc2DataTaylor(dataDisc, globM, globMDiscTaylor);
dataTaylor = applySlopeLimiterTaylor(g, dataTaylor, markV0TbdrD, dataV0T, type);
dataDisc = projectDataTaylor2DataDisc(dataTaylor, globM, globMDiscTaylor);
end
```

`dataTaylor = applySlopeLimiterTaylor(g, dataTaylor, markV0TbdrD, dataV0T, type)` implements the slope limiting operator $\mathbf{\Phi}^{\text{Taylor}}$, as described in Sec. 3.5. Parameter `dataTaylor` is the representation matrix in Taylor basis, the other parameters are the same as for `applySlopeLimiterDisc`.

```
function dataTaylorLim = applySlopeLimiterTaylor(g, dataTaylor, markV0TbdrD, dataV0T, type)
switch type
  case 'linear'
    dataTaylorLim = applySlopeLimiterTaylorLinear(g, dataTaylor, markV0TbdrD, dataV0T);
  case 'hierarch_vert'
    dataTaylorLim = applySlopeLimiterTaylorHierarchicalVertex(g, dataTaylor, markV0TbdrD, dataV0T);
  case 'strict'
    dataTaylorLim = applySlopeLimiterTaylorStrict(g, dataTaylor, markV0TbdrD, dataV0T);
  otherwise
    error('Unknown limiter type');
end
end
```

`dataTaylorLim = applySlopeLimiterTaylorHierarchicalVertex(g, dataTaylor, markV0TbdrD, dataV0T)` applies the hierarchical vertex-based limiter as described in Sec. 3.3, with input parameters as for `applySlopeLimiterTaylor`.

```
function dataTaylorLim = applySlopeLimiterTaylorHierarchicalVertex(g, dataTaylor, markV0TbdrD, dataV0T)
global gPhiTaylorV0T
[K, N] = size(dataTaylor); p = (sqrt(8*N+1)-3)/2;
dataTaylorLim = zeros(size(dataTaylor)); dataTaylorLim(:, 1) = dataTaylor(:, 1);
alpha = zeros(K, 1);
for ord = p : -1 : 1
  alphaOrd = ones(K, 1);
  indDOF = ord*(ord+1)/2 + 1 : (ord+1)*(ord+2)/2;
  for i = 1 : ord
    mult = bsxfun(@plus, [ord - i, i - 1], multiindex(1));
    ind = mult2ind(mult);
    valV0T = computeFuncDiscAtPoints(dataTaylor(:, ind), gPhiTaylorV0T(:, :, 1:3));
    if ord > 1
      alphaTmp = computeVertexBasedLimiter(g, dataTaylor(:, ind(1)), valV0T, markV0TbdrD, valV0T);
    else
      alphaTmp = computeVertexBasedLimiter(g, dataTaylor(:, ind(1)), valV0T, markV0TbdrD, dataV0T);
    end
    alphaOrd = min(alphaOrd, alphaTmp);
  end
  alpha = max(alpha, alphaOrd);
  dataTaylorLim(:, indDOF) = bsxfun(@times, alpha, dataTaylor(:, indDOF));
end
end % function
```

`dataTaylorLim = applySlopeLimiterTaylorLinear(g, dataTaylor, markV0TbdrD, dataV0T)` applies the linear vertex-based limiter as described in Sec. 3.2, with input parameters as for `applySlopeLimiterTaylor`.

```
function dataTaylorLim = applySlopeLimiterTaylorLinear(g, dataTaylor, markV0TbdrD, dataV0T)
global gPhiTaylorV0T
alphaE = computeVertexBasedLimiter(g, dataTaylor(:, 1), computeFuncDiscAtPoints(dataTaylor(:, 1:3),
    ↪gPhiTaylorV0T(:,:,1:3)), markV0TbdrD, dataV0T);
dataTaylorLim = [dataTaylor(:,1), bsxfun(@times, alphaE, dataTaylor(:, 2:3)), bsxfun(@times, alphaE ==
    ↪1, dataTaylor(:, 4:end))];
end % function
```

`dataTaylorLim = applySlopeLimiterTaylorStrict(g,dataTaylor, markV0TbdrD, dataV0T)` applies the stricter form of the hierarchical vertex-based limiter as described in Sec. 3.4, with input parameters as for `applySlopeLimiterTaylor`.

```
function dataTaylorLim = applySlopeLimiterTaylorStrict(g, dataTaylor, markV0TbdrD, dataV0T)
global gPhiTaylorV0T
[K, N] = size(dataTaylor); p = (sqrt(8*N+1)-3)/2;
dataTaylorLim = dataTaylor;
for ord = p : -1 : 1
  alphaOrd = ones(K, 1);
  indDOF = ord * (ord + 1) / 2 + 1 : N;
  for i = 1 : ord
    pReconstruction = p - ord + 1;
    mult = bsxfun(@plus, [ord - i, i - 1], multiindex(pReconstruction)); ind = mult2ind(mult);
    valV0T = computeFuncDiscAtPoints(dataTaylorLim(:, ind), gPhiTaylorV0T(:, :, 1 : size(ind, 1)));
    if ord > 1
      alphaTmp = computeVertexBasedLimiter(g, dataTaylorLim(:, ind(1)), valV0T, markV0TbdrD, valV0T);
    else
      alphaTmp = computeVertexBasedLimiter(g, dataTaylorLim(:, ind(1)), valV0T, markV0TbdrD, dataV0T);
    end
    alphaOrd = min(alphaOrd, alphaTmp);
  end
  dataTaylorLim(:, indDOF) = bsxfun(@times, alphaOrd, dataTaylorLim(:, indDOF));
end
end % function
```

`ret = assembleMatEdgePhiPhiValUpwind(g, refEdgePhiIntPhiInt, refEdgePhiIntPhiExt, valOnQuad)` assembles the matrix $\mathbf{R}$ according to Sec. 4.3.3, containing edge integrals of products of two basis functions multiplied with for each quadrature point specified values, stored in `valOnQuad`, and where the upwind-sided value w. r. t. `valOnQuad` is chosen. The input arguments `refEdgePhiIntPhiInt` and `refEdgePhiIntPhiExt` provide the local matrices $\hat{\mathbf{R}}^{\text{diag}}$ and $\hat{\mathbf{R}}^{\text{offdiag}}$ (multidimensional arrays), respectively.

```
function ret = assembleMatEdgePhiPhiValUpwind(g, refEdgePhiIntPhiIntOnQuad, refEdgePhiIntPhiExtOnQuad,
    ↪valOnQuad)
K = g.numT; N = size(refEdgePhiIntPhiIntOnQuad, 1);
ret = sparse(K*N, K*N);
p = (sqrt(8*N+1)-3)/2;
qOrd = 2*p+1;  [~, W] = quadRule1D(qOrd);
for nn = 1 : 3
  Rkn = g.areaE0T(:, nn);
  for r = 1 : length(W)  % Diagonal blocks
    ret = ret + kron(spdiags(W(r) .* Rkn .* valOnQuad(:, nn, r) .* (valOnQuad(:, nn, r) > 0), 0, K, K),
        ↪refEdgePhiIntPhiIntOnQuad(:, :, nn, r));
  end
  for np = 1 : 3  % Off-diagonal blocks
    RknTimesVal = sparse(K*N, N);
    for r = 1 : length(W)
      RknTimesVal = RknTimesVal + kron(W(r) .* Rkn .* valOnQuad(:, nn, r) .* sparse(valOnQuad(:, nn, r)
          ↪< 0), refEdgePhiIntPhiExtOnQuad(:, :, nn, np, r));
    end
    ret = ret + kronVec(g.markE0TE0T{nn, np}, RknTimesVal);
  end % for
end % for
end % function
```

`ret = assembleMatElemDphiPhiFuncDiscVec(g, refElemDphiPhiPhi, dataDisc1, dataDisc2)` assembles two matrices, each containing integrals of products of a basis function with a (spatial) derivative of a basis function and with a component of a discontinuous coefficient function whose coefficients are specified in `dataDisc1` and `dataDisc2`, respectively. The matrices are returned in a 2×1 `cell` variable. This corresponds to the matrices $\mathbf{G}^m$, $m \in \{1, 2\}$ according to Sec. 4.3.2. The input argument `refElemDphiPhiPhi` stores the local matrices $\hat{\mathbf{G}}$ (multidimensional array) as defined in (37) and can be computed by `integrateRefElemDphiPhiPhi` [3]. The coefficients of the projection of the algebraic diffusion coefficient d into the broken polynomial space are stored in the input arguments `dataDisc1` and `dataDisc2` and can be computed by `projectFuncCont2dataDisc`.

```
function ret = assembleMatElemDphiPhiFuncDiscVec(g, refElemDphiPhiPhi, dataDisc1, dataDisc2)
[K, N] = size(dataDisc1);
ret = cell(2, 1);  ret{1} = sparse(K*N, K*N);  ret{2} = sparse(K*N, K*N);
for l = 1 : N
  ret{1} = ret{1} + kron(spdiags(dataDisc1(:,l) .* g.B(:,2,2), 0,K,K), refElemDphiPhiPhi(:,:,l,1)) ...
```

```
                - kron(spdiags(dataDisc1(:,1) .* g.B(:,2,1), 0,K,K), refElemDphiPhiPhi(:,:,1,2));
  ret{2} = ret{2} - kron(spdiags(dataDisc2(:,1) .* g.B(:,1,2), 0,K,K), refElemDphiPhiPhi(:,:,1,1)) ...
                + kron(spdiags(dataDisc2(:,1) .* g.B(:,1,1), 0,K,K), refElemDphiPhiPhi(:,:,1,2));
end % for
end % function
```

`ret = assembleMatElemPhiDiscPhiTaylor(g, N)` assembles the matrix $\mathbf{M}^{\mathrm{DG,Taylor}}$ according to Sec. 3.1, which corresponds to the basis transformation matrix with one basis function from each, modal and Taylor basis. It is required for the transformation between modal and Taylor basis in the routines `projectDataDisc2DataTaylor` and `projectDataTaylor2DataDisc`.

```
function ret = assembleMatElemPhiDiscPhiTaylor(g, N)
global gPhi2D
p = (sqrt(8*N+1)-3)/2;  qOrd = max(2*p+1, 1);  [Q1,Q2,W] = quadRule2D(qOrd);
K = g.numT; ret = sparse(K*N, K*N);
for i = 1 : N
  for j = 1 : N
    intPhiIPhiJ =  ( repmat(gPhi2D{qOrd}(:, i)', [K 1]) .* phiTaylorRef(g, j, Q1, Q2) ) * W';
    ret = ret + sparse(i : N : K*N, j : N : K*N, 2 * g.areaT .* intPhiIPhiJ, K*N, K*N );
  end % for
end % for
end % function
```

`ret = assembleMatElemPhiTaylorPhiTaylor(g, N)` assembles the mass matrix in Taylor basis $\mathbf{M}^{\mathrm{Taylor}}$.

```
function ret = assembleMatElemPhiTaylorPhiTaylor(g, N)
p = (sqrt(8*N+1)-3)/2;  qOrd = max(2*p, 1);
[Q1, Q2, W] = quadRule2D(qOrd);
K = g.numT;
ret = sparse(K*N, K*N);
for i = 1 : N
  for j = 1 : N
    intPhiIPhiJ =  ( phiTaylorRef(g, i, Q1, Q2) .* phiTaylorRef(g, j, Q1, Q2) ) * W';
    ret = ret + sparse(i : N : K*N, j : N : K*N, 2 * g.areaT .* intPhiIPhiJ, K*N, K*N );
  end % for
end % for
end % function
```

`ret = assembleVecEdgePhiIntFuncContVal(g, markE0Tbdr, funcCont, valOnQuad, N)` assembles a vector containing integrals of products of a basis function with a continuous function and a given value that is provided in each quadrature point on each edge for all triangles. This corresponds to the contributions of Dirichlet boundaries $\boldsymbol{K}_{\mathrm{D}}$ to the right-hand side of (4) according to Sec. 4.3.4. `markE0Tbdr` marks the boundary edges on which the vector should be assembled, `funcCont` is a function handle and `valOnQuad` is the value provided in each quadrature point, as computed by `computeFuncContNuOnQuadEdge`.

```
function ret = assembleVecEdgePhiIntFuncContVal(g, markE0Tbdr, funcCont, valOnQuad, N)
global gPhi1D
K = g.numT;  p = (sqrt(8*N+1)-3)/2; qOrd = 2*p+1;  [Q, W] = quadRule1D(qOrd);
Q2X1 = @(X1,X2) g.B(:,1,1)*X1 + g.B(:,1,2)*X2 + g.coordV0T(:,1,1)*ones(size(X1));
Q2X2 = @(X1,X2) g.B(:,2,1)*X1 + g.B(:,2,2)*X2 + g.coordV0T(:,1,2)*ones(size(X1));
ret = zeros(K, N);
for n = 1 : 3
  [Q1, Q2] = gammaMap(n, Q);  funcOnQuad = funcCont(Q2X1(Q1, Q2), Q2X2(Q1, Q2));
  Kkn = markE0Tbdr(:, n) .* g.areaE0T(:,n);
  for i = 1 : N
    integral = (funcOnQuad .* squeeze((valOnQuad(:, n, :) < 0) .* valOnQuad(:, n, :))) * ( W' .* gPhi1D{
        ↪qOrd}(:,i,n));
    ret(:,i) = ret(:,i) + Kkn .* integral;
  end % for
end % for
ret = reshape(ret',K*N,1);
end % function
```

`ret = computeFuncContNuOnQuadEdge(g, funcCont1, funcCont2, qOrd)` assembles a three-dimensional array with the normal velocity $\boldsymbol{u} \cdot \boldsymbol{\nu}_{ki}$ evaluated in all quadrature points of all edges of each triangle.

```
function ret = computeFuncContNuOnQuadEdge(g, funcCont1, funcCont2, qOrd)
K = g.numT;  [Q, W] = quadRule1D(qOrd);
```

```
ret = zeros(K, 3, length(W));
for n = 1 : 3
  [Q1, Q2] = gammaMap(n, Q);
  ret(:,n,:) = bsxfun(@times,g.nuE0T(:,n,1),funcCont1(g.mapRef2Phy(1,Q1,Q2),g.mapRef2Phy(2,Q1,Q2)))+...
               bsxfun(@times,g.nuE0T(:,n,2),funcCont2(g.mapRef2Phy(1,Q1,Q2),g.mapRef2Phy(2,Q1,Q2)));
end % for
end
```

`valV0T = computeFuncContV0T(g, funcCont)` assembles a matrix containing the function `funcCont` evaluated in each node of each triangle.

```
function valV0T = computeFuncContV0T(g, funcCont)
valV0T = zeros(g.numT,3);
for n = 1 : 3
    valV0T(:, n) = funcCont(g.coordV0T(:, n, 1), g.coordV0T(:, n, 2));
end
end
```

`ret = computeFuncDiscAtPoints(funcDisc, phiAtPoints)` assembles a matrix containing the values of a discrete function with representation matrix stored in `funcDisc` evaluated in all points, for which the evaluated basis functions are given in `phiAtPoints`.

```
function ret = computeFuncDiscAtPoints(funcDisc, phiAtPoints)
nPoints = size(phiAtPoints, 2); K = size(funcDisc, 1);
ret = zeros(K, nPoints);
for i = 1 : nPoints
  ret(:, i) = sum(funcDisc .* squeeze(phiAtPoints(:, i, :)), 2);
end %for
end % function
```

`minMaxV0T = computeMinMaxV0TElementPatch(g, valCentroid, markV0TbdrD, dataV0T)` determines a matrix with bounds $c_{ki}^{\max}$, $c_{ki}^{\min}$ of Eq. (22) for each vertex of each triangle, as required by `computeVertexBasedLimiter`.

```
function minMaxV0T = computeMinMaxV0TElementPatch(g, valCentroid, markV0TbdrD, dataV0T)
minMaxV0T = cell(2,1);
minMaxV0T{1} = zeros(g.numT, 3); minMaxV0T{2} = zeros(g.numT, 3);
shiftCentroidPos = abs(min(valCentroid)) + 1;
shiftCentroidNeg = abs(max(valCentroid)) + 1;
valCentroidPos = valCentroid + shiftCentroidPos;
valCentroidNeg = valCentroid - shiftCentroidNeg;
valD = NaN(g.numT, 3); valD(markV0TbdrD) = dataV0T(markV0TbdrD);
for i = 1 : 3
  markNbV0T = g.markV0TV0T{i, 1} | g.markV0TV0T{i, 2} | g.markV0TV0T{i, 3};
  if exist('OCTAVE_VERSION','builtin')
    markNbV0T = markNbV0T + 0 * speye(size(markNbV0T, 1), size(markNbV0T, 2));
  end
  minMaxV0T{1}(:,i)=min(min(bsxfun(@times,markNbV0T,valCentroidNeg'),[],2)+shiftCentroidNeg,valD(:,i));
  minMaxV0T{2}(:,i)=max(max(bsxfun(@times,markNbV0T,valCentroidPos'),[],2)-shiftCentroidPos,valD(:,i));
end % for
end % function
```

`computeTaylorBasesV0T(g, N)` evaluates the Taylor basis functions Φ_{kj} in all vertices of all triangles $\boldsymbol{x}_{ki}$ and stores them in a global multidimensional array.

```
function computeTaylorBasesV0T(g, N)
global gPhiTaylorV0T
gPhiTaylorV0T = zeros(g.numT, 3, N);
for n = 1 : 3
  for i = 1 : N
    gPhiTaylorV0T(:, n, i) = phiTaylorPhy(g, i, g.coordV0T(:, n, 1), g.coordV0T(:, n, 2));
  end
end
end
```

`alphaE = computeVertexBasedLimiter(g, valCentroid, valV0T, markV0TbdrD, dataV0T)` computes a vector with correction factors α_{ke} (cf. Eq. (23)) for all elements. Centroid values c_{kc} are given in `valCentroid`, values of the unconstrained reconstruction c_{ki} are specified in `valV0T` and `markV0TbdrD` is a logical matrix marking all Dirichlet boundary nodes for which boundary data is given in `dataV0T`.

```
function alphaE = computeVertexBasedLimiter(g, valCentroid, valV0T, markV0TbdrD, dataV0T)
minMaxV0T = computeMinMaxV0TElementPatch(g, valCentroid, markV0TbdrD, dataV0T);
diffV0TCentroid = valV0T - repmat(valCentroid, [1 3]);
diffMinCentroid = minMaxV0T{1} - repmat(valCentroid, [1 3]);
diffMaxCentroid = minMaxV0T{2} - repmat(valCentroid, [1 3]);
tol = 1.e-8;
markNeg = diffV0TCentroid < diffMinCentroid + tol;
markPos = diffV0TCentroid > diffMaxCentroid - tol;
alphaEV0T = ones(g.numT,3);
alphaEV0T(markNeg) = max(0, min(1, diffMinCentroid(markNeg) ./ (diffV0TCentroid(markNeg) - tol) ) );
alphaEV0T(markPos) = max(0, min(1, diffMaxCentroid(markPos) ./ (diffV0TCentroid(markPos) + tol) ) );
alphaE = min(alphaEV0T,[],2);
end % function
```

`ret = integrateRefEdgePhiIntPhiExtPerQuad(N)` computes a multidimensional array of functionals in the quadrature points on the edges of the reference triangle $\hat{T}$ that consist of all permutations of two basis functions of which one belongs to a neighboring element that is transformed using $\hat{\boldsymbol{\vartheta}}$. This corresponds to the local matrix $\hat{\mathbf{R}}^{\text{offdiag}}$ as given in (40).

```
function ret = integrateRefEdgePhiIntPhiExtPerQuad(N)
global gPhi1D gThetaPhi1D
p = (sqrt(8*N+1)-3)/2;  qOrd = 2*p+1;  [~, W] = quadRule1D(qOrd);
ret = zeros(N,N,3,3,length(W)); % [N x N x N x 3 x 3]
for nn = 1 : 3 % 3 edges
  for np = 1 : 3
      for i = 1 : N
        for j = 1 : N
          ret(i, j, nn, np, :) = gPhi1D{qOrd}(:,i,nn) .* gThetaPhi1D{qOrd}(:,j,nn,np);
        end % for
      end % for
  end % for
end % for
end
```

`ret = integrateRefEdgePhiIntPhiIntPerQuad(N)` computes a multidimensional array of functionals in the quadrature points on the edges of the reference triangle $\hat{T}$ that consist of all permutations of two basis functions. This corresponds to the local matrix $\hat{\mathbf{R}}^{\text{diag}}$ as given in (38).

```
function ret = integrateRefEdgePhiIntPhiIntPerQuad(N)
global gPhi1D
p = (sqrt(8*N+1)-3)/2;  qOrd = max(2*p+1,1);  [~, W] = quadRule1D(qOrd);
ret = zeros(N, N, 3, length(W)); % [N x N x 3 x R]
for n = 1 : 3 % 3 edges
    for i = 1 : N
      for j = 1 : N
        ret(i,j,n,:) = gPhi1D{qOrd}(:,i,n).* gPhi1D{qOrd}(:,j,n);
      end % for
    end % for
end % for
end % function
```

`K = kronVec(A,B)` computes the result of $\mathbb{R}^{m_b \times n_a n_b} \ni \mathbf{K} = \mathbf{A} \otimes_{\mathrm{V}} \mathbf{B}$ as given in Eq. (41).

```
function K = kronVec(A, B)
[ma,na] = size(A);
[mb,nb] = size(B);
mc = mb / ma;
if ~issparse(A) && ~issparse(B) % Both inputs full, result is full.
  A = reshape(A, [1 ma 1 na]);
  B = reshape(B, [mc ma nb 1]);
  K = reshape(bsxfun(@times, A, B), [mb na*nb]);
else
  [i2, j2, v2] = find(kron(A, ones(mc, 1)));
  ik = repmat(i2, [1 nb]);
  jk = bsxfun(@plus, nb * (j2 - 1), 1 : nb);
  sk = bsxfun(@times, v2, B(i2, :));
  K = sparse(ik, jk, sk, mb, na * nb);
end % if
end % function
```

`mainAdvection.m` This is the main script to solve (1) which can be used as a template for further modifications. Modifiable parameters are found in Lines 5–16, the problem data (initial condition, velocity, right-hand side and boundary data) is specified in Lines 35–42.

```
function mainAdvection()
more off % disable paging of output
tic % Start time measurement
%% Parameters.
hmax         = 2^-6;              % maximum edge length of triangle
p            = 2;                 % local polynomial degree
ordRK        = min(p+1,3);        % order of Runge Kutta time stepper.
tEnd         = 2*pi;              % end time
numSteps     = 3142;              % number of time steps
isVisGrid    = false;             % visualization of grid
isVisSol     = true;              % visualization of solution
isSlopeLim   = true;              % slope limiting
typeSlopeLim = 'hierarch_vert';   % Type of slope limiter (linear, hierarch_vert, strict)
outputFrequency = 100;            % no visualization of every timestep
outputBasename  = ['solution_' typeSlopeLim]; % Basename of output files
outputTypes     = cellstr(['vtk';'tec']);
%% Parameter check.
diary([outputBasename '.log'])
assert(p >= 0 && p <= 4         , 'Polynomial order must be zero to four.'     )
assert(ordRK >= 1 && ordRK <= 3, 'Order of Runge Kutta must be zero to three.')
assert(hmax > 0                 , 'Maximum edge length must be positive.'      )
assert(numSteps > 0             , 'Number of time steps must be positive.'     )
assert(~isSlopeLim || p > 0     , 'Slope limiting only available for p > 0.'   )
%% Triangulation.
g = domainSquare(hmax); % Alternative: g = domainPolygon([0 1 1 0], [0 0 1 1], hmax);
if isVisGrid,  visualizeGrid(g);  end
%% Globally constant parameters.
K           = g.numT;                       % number of triangles
N           = nchoosek(p + 2, p);           % number of local DOFs
tau         = tEnd/numSteps;                % time step size
markE0Tint  = g.idE0T == 0;                 % [K x 3] mark local edges that are interior
markE0TbdrD = ~markE0Tint;                  % [K x 3] mark local edges on the Dirichlet boundary
markV0TbdrD = ismember(g.V0T, g.V0E(g.E0T(markE0TbdrD),:)); % [K x 3] mark vertices on Dirichlet bdr
%% Coefficients and boundary data (LeVeque's solid body rotation).
G = @(x1, x2, x1_0, x2_0) (1/0.15) * sqrt((x1-x1_0).^2 + (x2-x2_0).^2);
c0Cont = @(x1, x2) ((x1-0.5).^2+(x2-0.75).^2 <= 0.0225 & (x1<=0.475|x1>=0.525|x2>=0.85)) + ...
                    (1-G(x1, x2, 0.5, 0.25)) .* ((x1 - 0.5).^2 + (x2 - 0.25).^2 <= 0.0225) + ...
                  0.25*(1+cos(pi*G(x1, x2, 0.25, 0.5))).*((x1 - 0.25).^2 + (x2 - 0.5).^2 <= 0.0225);
fCont = @(t,x1,x2) zeros(size(x1));
u1Cont = @(t,x1,x2) 0.5 - x2;
u2Cont = @(t,x1,x2) x1 - 0.5;
cDCont = @(t,x1,x2) zeros(size(x1));
%% Lookup table for basis function.
computeBasesOnQuad(N);
if isSlopeLim, computeTaylorBasesV0T(g, N); end
%% Computation of matrices on the reference triangle.
hatM              = integrateRefElemPhiPhi(N);
hatG              = integrateRefElemDphiPhiPhi(N);
hatRdiagOnQuad    = integrateRefEdgePhiIntPhiIntPerQuad(N);
hatRoffdiagOnQuad = integrateRefEdgePhiIntPhiExtPerQuad(N);
%% Assembly of time-independent global matrices.
globM  = assembleMatElemPhiPhi(g, hatM);
if isSlopeLim
  globMTaylor     = assembleMatElemPhiTaylorPhiTaylor(g, N);
  globMDiscTaylor = assembleMatElemPhiDiscPhiTaylor(g, N);
  globMCorr       = spdiags(1./diag(globMTaylor), 0, K*N, K*N) * globMTaylor;
end % if
%% Initial data.
cDisc = projectFuncCont2DataDisc(g, c0Cont, 2*p+1, hatM);
if isSlopeLim
  cDV0T = computeFuncContV0T(g, @(x1, x2) cDCont(0, x1, x2));
  cDisc = applySlopeLimiterDisc(g, cDisc, markV0TbdrD, cDV0T, globM, globMDiscTaylor, typeSlopeLim);
end % if
fprintf('L2 error w.r.t. the initial condition: %g\n', computeL2Error(g, cDisc, c0Cont, 2*p));
%% visualization of inital condition.
if isVisSol
  cLagrange = projectDataDisc2DataLagr(cDisc);
  visualizeDataLagr(g, cLagrange, 'u_h', outputBasename, 0, outputTypes)
end
%% Time stepping.
fprintf('Starting time integration from 0 to %g using time step size %g (%d steps).\n', tEnd, tau,
    ↪numSteps)
for nStep = 1 : numSteps
```

```
  [t, omega] = rungeKuttaSSP(ordRK, tau, (nStep - 1) * tau);
  cDiscRK = cell(length(omega)+1, 1); cDiscRK{1} = reshape(cDisc', [K*N 1]);
  %% Perform Runge-Kutta steps
  for rkStep = 1 : length(omega)
    % L2 projections of Contebraic coefficients
    fDisc  = projectFuncCont2DataDisc(g, @(x1,x2) fCont(t(rkStep),x1,x2),  2*p, hatM);
    u1Disc = projectFuncCont2DataDisc(g, @(x1,x2) u1Cont(t(rkStep),x1,x2), 2*p, hatM);
    u2Disc = projectFuncCont2DataDisc(g, @(x1,x2) u2Cont(t(rkStep),x1,x2), 2*p, hatM);
    % Evaluate normal velocity in quadrature points of edges
    vNormalOnQuadEdge = computeFuncContNuOnQuadEdge(g, @(x1,x2) u1Cont(t(rkStep),x1,x2), @(x1,x2) u2Cont
        ↪(t(rkStep),x1,x2), 2*p+1); % veloc \dot \nu on quadratur points on edges
    % Assembly of time-dependent global matrices
    globG = assembleMatElemDphiPhiFuncDiscVec(g, hatG, u1Disc, u2Disc);
    globR = assembleMatEdgePhiPhiValUpwind(g, hatRdiagOnQuad, hatRoffdiagOnQuad, vNormalOnQuadEdge);
    % Assembly of Dirichlet boundary contributions
    globKD = assembleVecEdgePhiIntFuncContVal(g, markE0TbdrD, @(x1,x2) cDCont(t(rkStep),x1,x2),
        ↪vNormalOnQuadEdge, N);
    % Assembly of the source contribution
    globL = globM * reshape(fDisc', K*N, 1);
    % Building the system
    sysA = -globG{1} - globG{2} + globR;
    sysV = globL - globKD;
    % Computing the discrete time derivative
    cDiscDot = globM \ (sysV - sysA * cDiscRK{rkStep});
    % Apply slope limiting to time derivative
    if isSlopeLim
      cDiscDotTaylor = projectDataDisc2DataTaylor(reshape(cDiscDot, [N K])', globM, globMDiscTaylor);
      cDiscDotTaylorLim = applySlopeLimiterTaylor(g,cDiscDotTaylor,markV0TbdrD,NaN(K,3),typeSlopeLim);
      cDiscDotTaylor = reshape(cDiscDotTaylorLim', [K*N 1]) + globMCorr * reshape((cDiscDotTaylor -
          ↪cDiscDotTaylorLim)', [K*N 1]);
      cDiscDot = reshape(projectDataTaylor2DataDisc(reshape(cDiscDotTaylor, [N K])', globM,
          ↪globMDiscTaylor)', [K*N 1]);
    end
    % Compute next step
    cDiscRK{rkStep + 1} = omega(rkStep) * cDiscRK{1} + (1 - omega(rkStep)) * (cDiscRK{rkStep} + tau *
        ↪cDiscDot);
    % Limiting the solution
    if isSlopeLim
      cDV0T = computeFuncContV0T(g, @(x1, x2) cDCont(t(rkStep), x1, x2));
      cDiscRK{rkStep + 1} = reshape(applySlopeLimiterDisc(g, reshape(cDiscRK{rkStep + 1}, [N K])',
          ↪markV0TbdrD, cDV0T, globM, globMDiscTaylor, typeSlopeLim)', [K*N 1]);
    end % if
  end % for
  cDisc = reshape(cDiscRK{end}, N, K)';
  %% visualization
  if isVisSol && mod(nStep, outputFrequency) == 0
    cLagrange = projectDataDisc2DataLagr(cDisc);
    visualizeDataLagr(g, cLagrange, 'u_h', outputBasename, nStep, outputTypes);
  end
end % for
if isVisSol
  cLagrange = projectDataDisc2DataLagr(cDisc);
  visualizeDataLagr(g, cLagrange, 'u_h', outputBasename, nStep, outputTypes);
end
fprintf('L2␣error␣w.r.t.␣the␣initial␣condition:␣%g\n', computeL2Error(g, cDisc, c0Cont, 2*p));
fprintf('Total␣computation␣time:␣%g␣seconds.\n', toc);
diary off
end % function
```

`ind = mult2ind(a)` computes the linear index $I(\boldsymbol{a})$ corresponding to a two-dimensional multi-index $\boldsymbol{a}$ as defined in (16).

```
function ind = mult2ind(a)
  p = sum(a, 2);  N = p .* (p + 1) / 2;
  ind = N + 1 + a(:, 2);
end
```

`mult = multiindex(p)` computes all two-dimensional multi-indices involved in the representation of a polynomial solution of degree p and returns them in a $N \times 2$ array.

```
function mult = multiindex(p)
mult = zeros(p * (p+1) / 2, 2);
mult(1,:) = [0, 0];
for ord = 1 : p
```

```
  offset = ord * (ord+1) / 2;
  for i = 1 : ord + 1
    mult(offset + i, :) = mult(1, :) + [ord - i + 1, i - 1];
  end
end
end
```

`ret = phiTaylorPhy(g, i, X1, X2)` evaluates the ith basis function ϕ_i on each triangle $T \in \mathcal{T}_h$ (cf. Sec. 3.1) at points specified by a list of n x^1 coordinates `X1` $\in \mathbb{R}^{K\times n}$ and x^2 coordinates `X2` $\in \mathbb{R}^{K\times n}$.

```
function ret = phiTaylorPhy(g, i, X1, X2)
qOrd = ceil((sqrt(8*i+1)-3)/2);
[Q1, Q2, W] = quadRule2D(qOrd);
Q2X1 = @(X1, X2) g.B(:, 1, 1) * X1 + g.B(:, 1, 2) * X2 + g.coordV0T(:, 1, 1) * ones(size(X1));
Q2X2 = @(X1, X2) g.B(:, 2, 1) * X1 + g.B(:, 2, 2) * X2 + g.coordV0T(:, 1, 2) * ones(size(X1));
R = length(W); K = g.numT; numP = size(X1, 2);
dX1 = repmat(2 ./ (max(g.coordV0T(:,:,1),[],2) - min(g.coordV0T(:,:,1),[],2)), [1 numP]);
dX2 = repmat(2 ./ (max(g.coordV0T(:,:,2),[],2) - min(g.coordV0T(:,:,2),[],2)), [1 numP]);
switch i
  case 1 % (0,0)
    ret = ones(K, numP);
  case 2 % (1,0)
    ret = (X1-repmat(g.baryT(:,1), [1 numP]).*dX1;
  case 3 % (0,1)
    ret = (X2-repmat(g.baryT(:,2), [1 numP]).*dX2;
  case 4 % (2,0)
    ret = ( 0.5*(X1-repmat(g.baryT(:,1), [1 numP]) ).^2-...
          repmat( ( Q2X1(Q1,Q2)-repmat(g.baryT(:,1), [1 R]) ).^2 * W', [1 numP])).*(dX1.*dX1);
  case 5 % (1,1)
    ret = ( ( X1-repmat(g.baryT(:,1), [1 numP]) ) .* ( X2-repmat(g.baryT(:,2), [1 numP]))-...
                  repmat( 2 * ( ( Q2X1(Q1,Q2)-repmat(g.baryT(:,1), [1 R]) ) .* ...
                        ( Q2X2(Q1,Q2)-repmat(g.baryT(:,2), [1 R]) ) ) * W', [1 numP])).*(dX1.*dX2);
  case 6 % (0,2)
    ret = ( 0.5*(X2-repmat(g.baryT(:,2), [1 numP]) ).^2-...
          repmat( ( Q2X2(Q1,Q2)-repmat(g.baryT(:,2), [1 R]) ).^2 * W', [1 numP])).*(dX2.*dX2);
  case 7 % (3,0)
    ret = ( ( X1-repmat(g.baryT(:,1), [1 numP]) ).^3 / 6-...
          repmat( ( Q2X1(Q1,Q2)-repmat(g.baryT(:,1), [1 R]) ).^3 * W' / 3, [1 numP])).*dX1.^3;
  case 8 % (2,1)
    ret = ( 0.5*(X1-repmat(g.baryT(:,1), [1 numP]) ).^2 .* ( X2-repmat(g.baryT(:,2), [1 numP]))-...
          repmat( ( ( Q2X1(Q1,Q2)-repmat(g.baryT(:,1), [1 R]) ).^2 .* ...
                  ( Q2X2(Q1,Q2)-repmat(g.baryT(:,2), [1 R]) ) ) * W', [1 numP])).*(dX1.^2.*dX2);
  case 9 % (1,2)
    ret = ( 0.5*(X1-repmat(g.baryT(:,1), [1 numP]) ) .* ( X2-repmat(g.baryT(:,2), [1 numP]) ).^2-...
          repmat( ( ( Q2X1(Q1,Q2)-repmat(g.baryT(:,1), [1 R]) ) .* ...
                  ( Q2X2(Q1,Q2)-repmat(g.baryT(:,2), [1 R]) ).^2 ) * W', [1 numP])).*(dX1.*dX2.^2);
  case 10 % (0,3)
    ret = ( ( X2-repmat(g.baryT(:,2), [1 numP]) ).^3 / 6-...
          repmat( ( Q2X2(Q1,Q2)-repmat(g.baryT(:,2), [1 R]) ).^3 * W' / 3, [1 numP])).*dX2.^3;
  case 11 % (4,0)
    ret = ( ( X1-repmat(g.baryT(:,1), [1 numP]) ).^4 / 24-...
          repmat( ( Q2X1(Q1,Q2)-repmat(g.baryT(:,1), [1 R]) ).^4 * W' / 12, [1 numP])).*dX1.^4;
  case 12 % (3,1)
    ret = ( ( X1-repmat(g.baryT(:,1), [1 numP]) ).^3 .* ( X2-repmat(g.baryT(:,2), [1 numP]) ) / 6-...
          repmat( ( ( Q2X1(Q1,Q2)-repmat(g.baryT(:,1), [1 R]) ).^3 .* ...
                  ( Q2X2(Q1,Q2)-repmat(g.baryT(:,2), [1 R]) ) ) * W' / 3, [1 numP])).*(dX1.^3.*dX2);
  case 13 % (2,2)
    ret = ( ( X1-repmat(g.baryT(:,1), [1 numP]) ).^2 .* ( X2-repmat(g.baryT(:,2), [1 numP])).^2 / 4-...
          repmat( ( (Q2X1(Q1,Q2)-repmat(g.baryT(:,1), [1 R])).^2 .* ...
                  (Q2X2(Q1,Q2)-repmat(g.baryT(:,2), [1 R])).^2 ) * W'/2, [1 numP])).*(dX1.*dX2).^2;
  case 14 % (1,3)
    ret = ( ( X1-repmat(g.baryT(:,1), [1 numP]) ) .* ( X2-repmat(g.baryT(:,2), [1 numP])).^3 / 6-...
          repmat( ( (Q2X1(Q1,Q2)-repmat(g.baryT(:,1), [1 R]) ) .* ...
                  (Q2X2(Q1,Q2)-repmat(g.baryT(:,2), [1 R])).^3) * W'/3, [1 numP])).*(dX1.*dX2.^3);
  case 15 % (0,4)
    ret = ( ( X2-repmat(g.baryT(:,2), [1 numP]) ).^4 / 24-...
          repmat( ( Q2X2(Q1,Q2)-repmat(g.baryT(:,2), [1 R]) ).^4 * W' / 12, [1 numP])).*dX2.^4;
end % switch
end
```

`ret = phiTaylorRef(g, i, hatX1, hatX2)` evaluates the ith basis function ϕ_i on each triangle $T \in \mathcal{T}_h$ (cf. Sec. 3.1) at points specified by a list of $\hat{x}^1$ coordinates `hatX1` and $\hat{x}^2$ coordinates `hatX2`.

```
function ret = phiTaylorRef(g, i, hatX1, hatX2)
```

```
Q2X1 = @(X1, X2) g.B(:, 1, 1) * X1 + g.B(:, 1, 2) * X2 + g.coordV0T(:, 1, 1) * ones(size(X1));
Q2X2 = @(X1, X2) g.B(:, 2, 1) * X1 + g.B(:, 2, 2) * X2 + g.coordV0T(:, 1, 2) * ones(size(X1));
ret = phiTaylorPhy(g, i, Q2X1(hatX1, hatX2), Q2X2(hatX1, hatX2));
end
```

`dataTaylor = projectDataDisc2DataTaylor(dataDisc, globMDisc, globMDiscTaylor)` converts the representation matrix in the DG / modal basis to the respective representation matrix in a Taylor basis, both of size $K \times N$. It solves Eq. (20) for $\mathbf{C}^{\text{Taylor}}$.

```
function dataTaylor = projectDataDisc2DataTaylor(dataDisc, globMDisc, globMDiscTaylor)
[K, N] = size(dataDisc);
dataTaylor = reshape(globMDiscTaylor \ ( globMDisc * reshape(dataDisc', [K*N 1]) ), [N K])';
end % function
```

`dataDisc = projectDataTaylor2DataDisc(dataTaylor, globMDisc, globMDiscTaylor)` converts the representation matrix in the Taylor basis to the respective representation matrix in a DG / modal basis, both of size $K \times N$. It solves Eq. (20) for $\mathbf{C}^{\text{DG}}$.

```
function dataDisc = projectDataTaylor2DataDisc(dataTaylor, globMDisc, globMDiscTaylor)
[K, N] = size(dataTaylor);
dataDisc = reshape(globMDisc \ (globMDiscTaylor * reshape(dataTaylor', [K*N 1]) ), [N K])';
end % function
```

`[t, omega] = rungeKuttaSSP(ord, tau, nStep)` provides a list of time levels $t^{(i)} = t^n + \delta_i \Delta t^n$ and weights ω_i for the n-th time step `nStep` with time step size `tau` according to Sec. 2.4. The order of the Runge-Kutta method is given as parameter `ord`.

```
function [t, omega] = rungeKuttaSSP(ord, tau, t0)
switch ord
  case 1
    omega = 0;              t = t0;
  case 2
    omega = [0, 0.5];       t = t0 + [0, 1] * tau;
  case 3
    omega = [0, 3/4, 1/3]; t = t0 + [0, 1, 0.5] * tau;
end
end % function
```

6. Conclusion and Outlook

The second installment in the present paper series on implementing a MATLAB / GNU Octave toolbox introduced performance optimized techniques for dealing with linear advection operators, higher order Runge–Kutta time discretizations, and a range of slope limiters designed to support general order DG discretizations. Our future work plans include nonlinear advection operators and coupled systems of PDEs as well as multi-physics applications with corresponding coupling mechanisms.

Acknowledgments

The work of B. Reuter was supported by the German Research Foundation (DFG) under grant AI 117/1-1.

Index of notation

Symbol	Definition
$\overline{\cdot}$	Integral mean, $\overline{v} := \frac{1}{\lvert T\rvert}\int_T v(\boldsymbol{x})\,\mathrm{d}\boldsymbol{x}$, where $v : T \to \mathbb{R}$.
$\mathrm{diag}(\mathbf{A},\mathbf{B})$	$:= \begin{bmatrix}\mathbf{A} & \\ & \mathbf{B}\end{bmatrix}$, block-diagonal matrix with blocks $\mathbf{A}$, $\mathbf{B}$.
$\#\mathcal{M}$	Cardinality of a set $\mathcal{M}$.
$\boldsymbol{a}\cdot\boldsymbol{b}$	$:= \sum_{m=1}^{2} a_m b_m$, Euclidean scalar product in $\mathbb{R}^2$.
$\boldsymbol{\nabla}$	$:= [\partial_{x^1}, \partial_{x^2}]^{\mathrm{T}}$, spatial gradient in the physical domain Ω.
$\circ$	Composition of functions or Hadamard product.
$\otimes$	Kronecker product.
c	Concentration (scalar-valued unknown).
c^0	Concentration prescribed at initial time $t = 0$.
c_{D}	Concentration prescribed on the inflow boundary.
$\boldsymbol{C}$	$\in \mathbb{R}^{KN}$, representation vector of $c_h \in \mathbb{P}_p(\mathcal{T}_h)$ with respect to $\{\varphi_{kj}\}$.
$\boldsymbol{C}^{\mathrm{Taylor}}$	$\in \mathbb{R}^{KN}$, representation vector of $c_h \in \mathbb{P}_p(\mathcal{T}_h)$ with respect to $\{\phi_{kj}\}$.
$\delta_{[\mathrm{condition}]}$	$:= \{1$ if condition is true, 0 otherwise$\}$, Kronecker delta.
$\boldsymbol{e}_m$	mth unit vector.
E_{kn}, $\hat{E}_n$	nth edge of the physical triangle T_k, nth edge of the reference triangle $\hat{T}$.
$\mathcal{V}$, $\mathcal{E}$, $\mathcal{T}$	Sets of vertices, edges, and triangles.
$\mathcal{E}_\Omega$, $\mathcal{E}_{\partial\Omega}$	Set of interior edges, set of boundary edges.
f	Source / sink (scalar-valued coefficient function).
$\boldsymbol{F}_k$	Affine mapping from $\hat{T}$ to T_k.
h	Mesh fineness of $\mathcal{T}_h$.
h_T	$:= \mathrm{diam}(T)$, diameter of triangle $T \in \mathcal{T}_h$.
J	$:= (0, t_{\mathrm{end}})$, open time interval.
K	$:= \#\mathcal{T}_h$, number of triangles.
$\boldsymbol{\nu}$	Unit normal on $\partial\Omega$ pointing outward of Ω.
$\boldsymbol{\nu}_T$	Unit normal on ∂T pointing outward of T.
$\boldsymbol{\nu}_k$	$:= \boldsymbol{\nu}_{T_k}$.
$N = N_p$	$:= (p+1)(p+2)/2$, number of local degrees of freedom of $\mathbb{P}_p(T)$.
ω_r	Quadrature weight associated with $\hat{\boldsymbol{q}}_r$.
Ω, $\partial\Omega$	spatial domain in two dimensions, boundary of Ω.
$\partial\Omega_{\mathrm{in}}$, $\partial\Omega_{\mathrm{out}}$	inflow- and outflow boundaries, $\partial\Omega = \partial\Omega_{\mathrm{in}} \cup \partial\Omega_{\mathrm{out}}$.
p	$= (\sqrt{8N+1} - 3)/2$, polynomial degree.
φ_{ki}, $\hat{\varphi}_i$	ith hierarchical basis function on T_k, ith hierarchical basis function on $\hat{T}$.
ϕ_{ki}	ith Taylor basis function on T_k.
$\mathbb{P}_p(T)$	Space of polynomials on $T \in \mathcal{T}_h$ of degree at most p.
$\mathbb{P}_p(\mathcal{T}_h)$	$:= \{w_h : \overline{\Omega} \to \mathbb{R}\,;\, \forall T \in \mathcal{T}_h,\ w_h\lvert_T \in \mathbb{P}_p(T)\}$.
$\boldsymbol{\Phi}$	Slope limiting operator with respect to $\{\varphi_{kj}\}$.
$\boldsymbol{\Phi}^{\mathrm{Taylor}}$	Slope limiting operator with respect to $\{\phi_{kj}\}$.
$\hat{\boldsymbol{q}}_r$	rth quadrature point in $\hat{T}$.
R	Number of quadrature points.
$\mathbb{R}^+$, $\mathbb{R}_0^+$	Set of (strictly) positive real numbers, set of non-negative real numbers.
t	Time variable.
t^n	nth time level.
t_{end}	End time.
$\hat{\boldsymbol{\vartheta}}_{n^-n^+}$	Mapping from $\hat{E}_{n^-}$ to $\hat{E}_{n^+}$.
Δt^n	$:= t^{n+1} - t^n$, time step size.
T_k, ∂T_k	kth physical triangle, boundary of T_k.
$\hat{T}$	Bi-unit reference triangle.
$\boldsymbol{u}$	Velocity (vector-valued coefficient function).
$\boldsymbol{x}$	$= [x^1, x^2]^{\mathrm{T}}$, space variable in the physical domain Ω.
$\hat{\boldsymbol{x}}$	$= [\hat{x}^1, \hat{x}^2]^{\mathrm{T}}$, space variable in the reference triangle $\hat{T}$.
$\boldsymbol{x}_{kc}$	Centroid of the element $T_k \in \mathcal{T}_h$.
$\boldsymbol{x}_{ki}$	ith vertex of the physical triangle T_k.

References

[1] F. Frank, B. Reuter, V. Aizinger, FESTUNG—The Finite Element Simulation Toolbox for UNstructured Grids (2016). doi:10.5281/zenodo.46069.
URL http://www.math.fau.de/FESTUNG

[2] F. Frank, B. Reuter, FESTUNG: The Finite Element Simulation Toolbox for UNstructured Grids (2016).
URL https://github.com/FESTUNG
[3] F. Frank, B. Reuter, V. Aizinger, P. Knabner, FESTUNG: A MATLAB / GNU Octave toolbox for the discontinuous Galerkin method, Part I: Diffusion operator, Computers & Mathematics with Applications 70 (1) (2015) 11–46. doi:10.1016/j.camwa.2015.04.013.
[4] B. Cockburn, C. Shu, The local discontinuous Galerkin method for time-dependent convection–diffusion systems, SIAM Journal on Numerical Analysis 35 (6) (1998) 2440–2463. doi:10.1137/S0036142997316712.
[5] H. Reed, T. R. Hill, Triangular mesh methods for the neutron transport equation, Tech. Rep. LA-UR-73-479, Los Alamos Scientific Laboratory, NM (1973).
[6] C. Johnson, J. Pitkranta, An Analysis of the Discontinuous Galerkin Method for a Sacalar Hyperbolic Equation, Mathematics of Computation 46 (173) (1986) 1–26.
[7] D. Kuzmin, Slope limiting for discontinuous Galerkin approximations with a possibly non-orthogonal Taylor basis, International Journal for Numerical Methods in Fluids 71 (9) (2013) 1178–1190. doi:10.1002/fld.3707.
[8] S. Gottlieb, C.-W. Shu, Strong stability-preserving high-order time discretization methods, Math. Comp. 67 (221) (1998) 73–85. doi:10.1090/S0025-5718-98-00913-2.
[9] S. Gottlieb, C.-W. Shu, E. Tadmor, Strong stability-preserving high-order time discretization methods, SIAM Review 43 (1) (2001) 89–112.
[10] B. Cockburn, C.-W. Shu, TVB Runge-Kutta local projection discontinuous Galerkin finite element method for conservation laws. II. General framework, Mathematics of computation 52 (186) (1989) 411–435.
[11] L. Krivodonova, J. Xin, J.-F. Remacle, N. Chevaugeon, J. E. Flaherty, Shock detection and limiting with discontinuous galerkin methods for hyperbolic conservation laws, Applied Numerical Mathematics 48 (3) (2004) 323–338.
[12] S. Tu, S. Aliabadi, A slope limiting procedure in discontinuous galerkin finite element method for gasdynamics applications, International Journal of Numerical Analysis and Modeling 2 (2) (2005) 163–178.
[13] C. Michoski, C. Mirabito, C. Dawson, D. Wirasaet, E. Kubatko, J. Westerink, Adaptive hierarchic transformations for dynamically p-enriched slope-limiting over discontinuous galerkin systems of generalized equations, Journal of Computational Physics 230 (22) (2011) 8028 – 8056. doi:10.1016/j.jcp.2011.07.009.
[14] M. Yang, Z.-J. Wang, A parameter-free generalized moment limiter for high-order methods on unstructured grids, Adv. Appl. Math. Mech 1 (4) (2009) 451–480.
[15] X. Zhang, Y. Xia, C.-W. Shu, Maximum-principle-satisfying and positivity-preserving high order discontinuous Galerkin schemes for conservation laws on triangular meshes, J. Sci. Comput. 50 (1) (2012) 29–62. doi:10.1007/s10915-011-9472-8.
[16] D. Kuzmin, A vertex-based hierarchical slope limiter for adaptive discontinuous Galerkin methods, Journal of Computational and Applied Mathematics 233 (12) (2010) 3077–3085, Finite Element Methods in Engineering and Science (FEMTEC 2009). doi:10.1016/j.cam.2009.05.028.
[17] M. Yang, Z.-J. Wang, A parameter-free generalized moment limiter for high-order methods on unstructured grids, in: 47th AIAA Aerospace Sciences Meeting Including The New Horizons Forum and Aerospace Exposition, AIAA-2009-605. doi:10.2514/6.2009-605.
[18] K. Michalak, C. Ollivier-Gooch, Limiters for unstructured higher-order accurate solutions of the euler equations, in: 46th AIAA Aerospace Sciences Meeting and Exhibit, AIAA-2008-776. doi:10.2514/6.2008-776.
[19] H. Luo, J. D. Baum, R. Lhner, A discontinuous Galerkin method based on a Taylor basis for the compressible flows on arbitrary grids, Journal of Computational Physics 227 (20) (2008) 8875 – 8893. doi:10.1016/j.jcp.2008.06.035.
[20] V. Aizinger, A geometry independent slope limiter for the discontinuous Galerkin method, in: E. Krause, Y. Shokin, M. Resch, D. Krner, N. Shokina (Eds.), Computational Science and High Performance Computing IV, Vol. 115 of Notes on Numerical Fluid Mechanics and Multidisciplinary Design, Springer Berlin Heidelberg, 2011, pp. 207–217. doi:10.1007/978-3-642-17770-5_16.
[21] T. Barth, D. Jespersen, The design and application of upwind schemes on unstructuredmeshes, in: Proc. AIAA 27th Aerospace Sciences Meeting, Reno, 1989.
[22] R. Cools, An encyclopaedia of cubature formulas, Journal of Complexity 19 (3) (2003) 445–453. doi:10.1016/S0885-064X(03)00011-6.
[23] B. Cockburn, C.-W. Shu, The Runge–Kutta discontinuous Galerkin method for conservation laws V: multidimensional systems, J. Comput. Phys. 141 (2) (1998) 199–224. doi:10.1006/jcph.1998.5892.
[24] R. J. Leveque, High-resolution conservative algorithms for advection in incompressible flow, SIAM Journal on Numerical Analysis 33 (2) (1996) 627–665. doi:10.2307/2158391.
[25] L. Sorber, Kronecker product, MATLAB Central File Exchange. Retrieved October 30, 2015 (2010).
URL http://de.mathworks.com/matlabcentral/fileexchange/28889-kronecker-product